A&A 615, A148 (2018)
https://doi.org/10.1051/0004-6361/201730960

Astronomy & Astrophysics

The low-mass pre-main sequence population of Scorpius OB1*

Francesco Damiani

INAF - Osservatorio Astronomico di Palermo G.S.Vaiana, Piazza del Parlamento 1, 90134 Palermo, Italy
e-mail: damiani@astropa.inaf.it

Received 8 April 2017 / Accepted 4 April 2018

ABSTRACT

Context. The low-mass members of OB associations, expected to be a major component of their total population, are in most cases poorly studied because of the difficulty of selecting these faint stars in crowded sky regions. Our knowledge of many OB associations relies on only a relatively small number of massive members.
Aims. We study here the Sco OB1 association, with the aim of a better characterization of its properties, such as global size and shape, member clusters and their morphology, age and formation history, and total mass.
Methods. We use deep optical and near-infrared (NIR) photometry from the VPHAS+ and VVV surveys, over a wide area ($2.6° \times 2.6°$), complemented by *Spitzer* infrared (IR) data, and *Chandra* and XMM-Newton X-ray data. A new technique is developed to find clusters of pre-main sequence M-type stars using suitable color-color diagrams, complementing existing selection techniques using narrow-band Hα photometry or NIR and ultraviolet (UV) excesses, and X-ray data.
Results. We find a large population of approximately 4000 candidate low-mass Sco OB1 members whose spatial properties correlate well with those of Hα-emission, NIR-excess, UV-excess, and X-ray detected members, and unresolved X-ray emission. The low-mass population is spread among several interconnected subgroups: they coincide with the H_{II} regions G345.45+1.50 and IC4628, and the rich clusters NGC 6231 and Trumpler 24, with an additional subcluster intermediate between these two. The total mass of Sco OB1 is estimated to be ~8500 $M_{\odot}$. Indication of a sequence of star-formation events is found, from South (NGC 6231) to North (G345.45+1.50). We suggest that the diluted appearance of Trumpler 24 indicates that the cluster is now dissolving into the field, and that tidal stripping by NGC 6231 nearby contributes to the process.

Key words. open clusters and associations: individual: Sco OB1 – open clusters and associations: individual: NGC6231 – open clusters and associations: individual: Trumpler 24 – stars: pre-main sequence – X-rays: stars

1. Introduction

OB associations are groups of massive stars, often covering tens of square degrees on the sky. While their massive members have been intensively studied, low-mass members are generally poorly known. This is due more to the technical challenges involved in the identification of these relatively faint stars than to lack of scientific interest. Most OB associations are found at low galactic latitudes, projected against a crowded field-star background; they are several hundred parsecs away, so deep photometry is required to detect their low-mass members. These latter stars, supposedly coeval to the massive ones, must still be in their pre-main sequence (PMS) evolutionary phase, since O and early-B stars cannot be older than a few million years.

Dramatic advances were made in the last two decades with the advent of sensitive X-ray observations (especially with *Chandra* and XMM-Newton), since low-mass PMS stars are three to four orders of magnitude brighter in X-rays than older, main sequence (MS) stars of the same mass. Therefore, a cluster of PMS stars is very conspicuous in X-ray images against the field-star population. Several massive clusters, often found near the central, densest part of OB associations, were studied in X-rays, and their rich low-mass PMS population identified. Besides the Orion Nebula Cluster in Ori OB1 (Flaccomio et al. 2003a,b; Getman et al. 2005), we mention NGC 2264 in Mon OB1 (Ramírez et al. 2004; Simon & Dahm 2005; Flaccomio et al. 2006), NGC 6530 in Sgr OB1 (Damiani et al. 2004), NGC 6611 and NGC 6618 (M17) in Ser OB1 (Linsky et al. 2007; Guarcello et al. 2007; Broos et al. 2007), NGC 2362 (Damiani et al. 2006a), NGC 2244 in Mon OB2 (Rosette Nebula; Wang et al. 2008), NGC 6193 in Ara OB1 (Skinner et al. 2005), Trumpler 14 and 16 in Car OB1 (Albacete-Colombo et al. 2008; Townsley et al. 2011), Cyg OB2 (Albacete Colombo et al. 2007; Wright et al. 2014), NGC 1893 in Aur OB2 (Caramazza et al. 2008), Cep OB3 (Getman et al. 2006), NGC 6231 in Sco OB1 (Damiani et al. 2016), and several others; see Damiani (2010) for a review. In each case, hundreds of low-mass stars were found, and up to nearly 10 000 in extremely large regions like Carina. Comparative studies involving several clusters were also made by Feigelson et al. 2013, Getman et al. (2017), and Townsley et al. (2014, 2018). Studies of the initial-mass-function on a wide mass range, the total cluster census, star-formation history and other properties were made possible by these observations.

However, the long exposure times required, and the small field-of-view (FOV) of these X-ray instruments, compared to the large spatial size of the OB associations, imply that only the stellar population of their densest central parts could be studied in X-rays. Sensitive X-ray studies of low-mass stars across the entire size of an OB association are lacking, and not even practically feasible with current X-ray instruments.

Other valuable means of studying PMS populations spread over wide sky areas exist: for example, deep narrow-band Hα imaging surveys such as IPHAS (Drew et al. 2005) or its

* Full Tables B.1–B.3 are only available at the CDS via anonymous ftp to cdsarc.u-strasbg.fr (130.79.128.5) or via http://cdsarc.u-strasbg.fr/viz-bin/qcat?J/A+A/615/A148

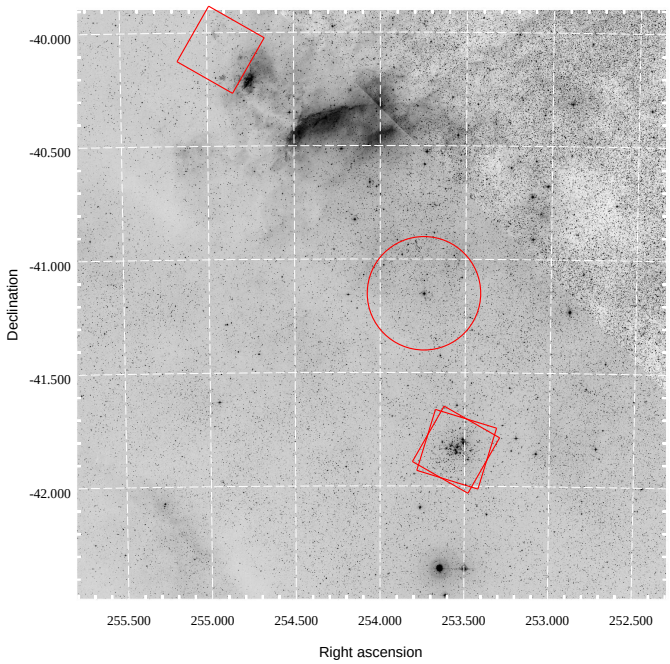

Fig. 1. Digital Sky Survey (DSS2, red band) image of the northern part of Sco OB1. The image size is 2.6° × 2.6° and coordinates are J2000. The FOVs of existing X-ray images are indicated with red squares (*Chandra*) and a circle (XMM-Newton). The massive cluster NGC 6231 is well visible inside the two southern *Chandra* fields. The northern *Chandra* field is centered on the IR source IRAS 16562-3959. Near the middle, the larger XMM-Newton FOV is centered on the Wolf-Rayet star WR79a, in the Tr 24 region. The bright nebula near top center is IC4628.

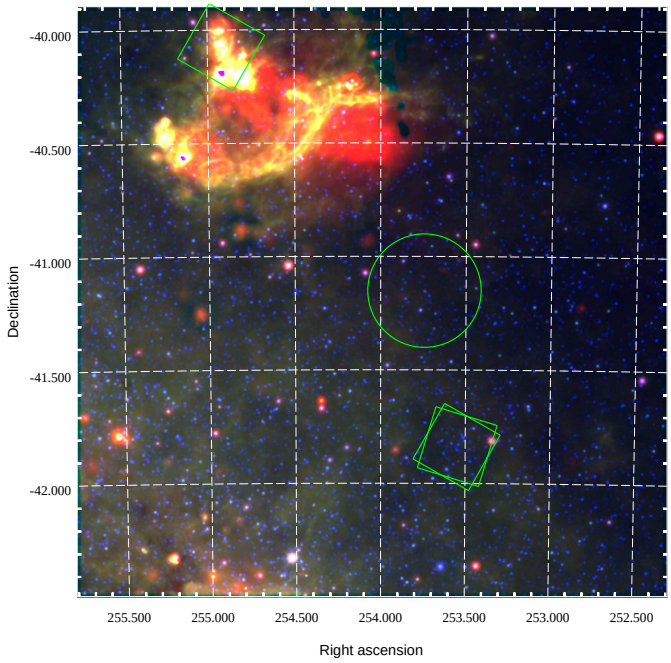

Fig. 2. WISE image of the same sky region as in Fig. 1, using bands at wavelengths 4.6μ (blue), 12μ (green), and 22μ (red). The same X-ray FOVs as in Fig. 1 are indicated as a reference. The bright diffuse emission coincides with the H_{II} region G345.45+1.50.

southern equivalent VPHAS+ (Drew et al. 2014) have the potential for uncovering all stars with strong Hα emission lines, including the classical T Tauri stars (CTTS), actively accreting PMS stars. Also the deep near-infrared (NIR) surveys of the galactic plane, such as the UKIDSS (Lawrence et al. 2007) or the VVV (Minniti et al. 2011) surveys are providing deep NIR catalogs, from which PMS stars with NIR emission excesses originating in circumstellar disks (Class II stars) can be found. Class II and CTTS stars (which largely overlap) constitute an important part of the low-mass content of star-formation regions and young PMS clusters, but rarely a dominant one. In fact, many PMS stars cease to accrete matter, and dissipate their disks within a few million years (Haisch et al. 2001), becoming Class III (or weak-line T Tauri, WTTS) stars well before the end of their PMS stage. These latter stars are still X-ray bright, possess active chromosphere and high lithium abundance, which are straightforward spectroscopic indicators of youth, but are difficult to find exclusively using optical and NIR photometry.

Our poor ability to identify PMS stars outside of dense clusters is a great obstacle in any study of the long-term evolution of a star-formation region, and of its past star-formation history. Lada & Lada (2003) argue that, on the basis of statistics of embedded and evolved clusters, the majority of young clusters dissolves already before 10 Myr. This implies that there must be huge numbers of low-mass PMS stars in the field (maybe 1/1000 of all field stars on the galactic plane). We are dramatically unable to find them, except serendipitously in spectroscopic studies of field stars. In the early years after the launch of the X-ray satellite ROSAT several studies were indicating that bright X-ray sources, found over hundreds square degrees around the Taurus-Auriga star-formation region, might be older PMS stars ejected from Tau-Aur and now dispersing in the field (Sterzik & Durisen 1995; Feigelson 1996). These studies were based on the ROSAT all-sky survey (RASS), which did not however have high enough sensitivity to study other, more distant star-formation regions like the vast majority of OB associations. Therefore, there is currently a significant lack of observational data on both the wide-area low-mass population of OB associations, and the possible halos of low-mass stars drifting away from star-formation regions, which may reveal their past star-formation histories.

In this work we explore an alternative method to those discussed above, able to distinguish the lowest-mass PMS population in and around a star-formation region of stars with M spectral type. This method exploits the properties of PMS M stars, and relies on deep, spatially uniform, multiband optical and NIR photometry, such as that offered by the VPHAS+ (or IPHAS or SDSS, for example) survey in the optical, complemented by deep NIR photometry if available. Despite the faintness of these stars, their study offers several advantages: they are the most numerous constituent of a star-formation region, and provide therefore a member sample with high statistics; and they have a small mass, and are most easily ejected from their parent cluster by dynamical interactions, thus probing its dynamical evolution. Finally, they constitute an unbiased sample with respect to the presence of accretion or circumstellar disks.

We study here the Sco OB1 association (Figs. 1 and 2), using this and other techniques. The general properties of this large OB association, which spans almost 5° on the sky, and is surrounded by a ring-shaped H_{II} region called Gum 55, are reviewed by Reipurth (2008). Its central cluster NGC 6231 contains several tens of OB stars, which have been extensively studied. On the other hand, many fewer studies, all recent, were devoted to the full mass spectrum, using optical photometry (Sung et al. 1998, 2013) and X-rays (Sana et al. 2006, 2007; Damiani et al. 2016; Kuhn et al. 2017a,b). The currently accepted

distance of NGC 6231 is approximately 1580 pc, and its age is between 2 and 8 Myr, with a significant intrinsic spread (Sung et al. 2013; Damiani et al. 2016). No ongoing star formation is known to occur therein, however. Approximately one degree North of the cluster, the loose cluster Trumpler 24 (Tr 24) also belongs to the association. There is little literature on this cluster (Seggewiss 1968; Heske & Wendker 1984, 1985; Fu et al. 2003, 2005) which unlike NGC 6231 lacks a well-defined center and covers about one square degree on the sky. Its age is <10 Myr according to Heske & Wendker (1984, 1985), who find several PMS stars, and its distance is 1570–1630 pc according to Seggewiss (1968). Other studies of the entire Sco OB1 association include MacConnell & Perry (1969 – Hα-emission stars), Schild et al. (1969 – spectroscopy), Crawford et al. (1971 – photometry), Laval (Laval 1972a,b – gas and star kinematics, respectively), van Genderen et al. (1984 – Walraven photometry), and Perry et al. (1991 – photometry). At the northern extreme of Sco OB1, the partially obscured H$_{II}$ region G345.45+1.50 and its less obscured neighbor IC4628 were studied by Laval (1972a), Caswell & Haynes (1987), López et al. (2011), and López-Calderón et al. (2016). They contain massive young stellar objects (YSOs; Mottram et al. 2007), maser sources (Avison et al. 2016), and the IRAS source 16562-3959 with its radio jet (Guzmán et al. 2010), outflow (Guzmán et al. 2011), and ionized wind (Guzmán et al. 2014), and are therefore extremely young (1 Myr or less). The distance of G345.45+1.50 was estimated as 1.9 kpc by Caswell & Haynes (1987), and 1.7 kpc by López et al. (2011), in fair agreement with distances of Sco OB1 stars. In Fig. 1 of Reipurth (2008) a strip of blue stars is visible, connecting NGC 6231 to the region of IC4628.

This paper is structured as follows: Sect. 2 describes the observational data used. Section 3 develops our techniques. Section 4 presents the results obtained. Section 5 is a discussion of their significance in a more general context, and Sect. 6 is a concluding summary.

2. Observational data

The spatial region selected for our study is a square of size $2.6^\circ \times 2.6^\circ$, centered on $(RA, Dec) = (254.05, -41.2)$ (J2000), that is $(l, b) = (344.19, 1.28)$. This region covers the northern half of Sco OB1, which comprises the vast majority of its OB stars, and the bright nebulous region to the north. The central cluster NGC 6231 is also included in our study.

Figure 2 shows the same region as in Fig. 1, as seen from the WISE observatory (Wright et al. 2010) in the IR: contrary to the optical image of Fig. 1, NGC is barely noticeable here, while a large structure of heated dust is seen to correspond to the H$_{II}$ region G345.45+1.50 and the optical nebula IC 4628. One of the brightest parts in the WISE image coincides with the source IRAS 16562-3959, targeted by a *Chandra* observation. The diffuse reddish emission in the southeast part of the WISE image corresponds to the Galactic Plane and is probably not related to Sco OB1, being typical of the Galactic equator.

We primarily use optical photometric data here from the VPHAS+ survey (*ugri* and Hα bands), and NIR photometry from the 2MASS and VVV surveys (*JHK* bands). These are nearly spatially complete over the region studied. In addition, we use photometry from the *Spitzer* Glimpse survey (Spitzer Science Center 2009), and X-ray data from the archives of *Chandra* and XMM-Newton observatories, which, as seen from Fig. 1, cover only a very small fraction of the studied region.

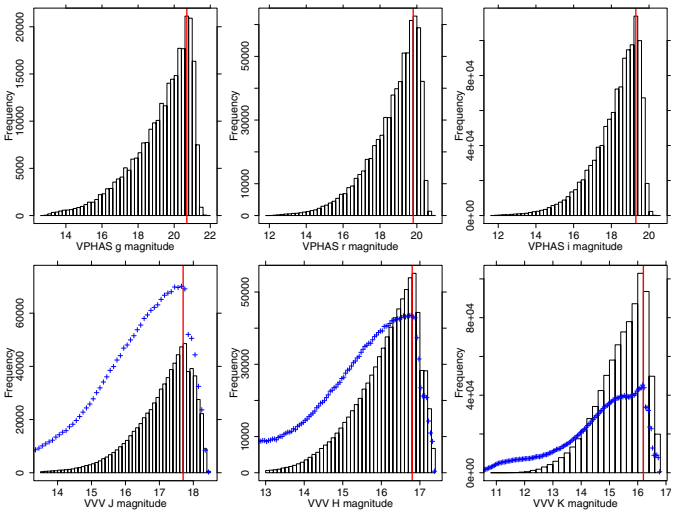

Fig. 3. Magnitude histograms for VPHAS+ bands g, r, i (*top panels*) and VVV bands J, H, K (*bottom panels*). The vertical red lines indicate our adopted completeness limits. In the *bottom panels*, the magnitude distributions of VVV catalog entries discarded because of non-zero *ppErrBits* flags are indicated by blue symbols.

2.1. Optical and NIR data

In the studied region, the VPHAS+ DR2 data comprise 2014322 individual sources with at least one of flags *clean_u, clean_g, clean_r, clean_i, clean_Hα* equal to 1 (i.e., a good and reliable magnitude in the given band). Individual *ugri* and Hα magnitudes were discarded when the corresponding *clean* flag is zero, but the source itself is not discarded if it has a good measurement in another of the VPHAS+ bands. The VPHAS+ data miss stars brighter than $i \sim 12$, which in Sco OB1 correspond to massive stars (above 4 $M_\odot$), thoroughly studied in the literature; since the emphasis here is on low-mass Sco OB1 members, this limitation has no consequences on our study. Histograms of the VPHAS+ source magnitudes in the *gri* bands are shown in Fig. 3 (top panels). From these we determine completeness limits of $g = 20.7$, $r = 19.8$, and $i = 19.3$, respectively. In regions with nebulosity the local limiting magnitude may be slightly brighter, depending on the nebular intensity in the given band, because of the increased background level. This might be of some consequence only in the vicinity of IC 4628 (Fig. 1), but for most of the studied region the VPHAS+ limiting magnitudes are spatially uniform. The spatial completeness of these optical data across the region is examined in detail in Sect. 4.

We used NIR data from VVV DR4 (table *vvvSource*), selecting only sources with stellar or probably stellar characteristics (flag *mergedClass* equal to −1 or −2). These comprise 8142990 sources, of which only the J, H, and K_s band magnitudes are considered here (we disregarded VVV Y and Z bands as they were not useful for this study). However, tests on NIR color-magnitude and color-color diagrams showed thousands of sources falling in unexpected places, and most likely having spurious colors. These were generally found to possess flags *jppErrBits* > 0, *hppErrBits* > 0, or *ksppErrBits* > 0. We therefore disregarded all magnitudes with the corresponding flag set to a nonzero value. This is a stronger filtering than suggested in the VVV DR4 explanatory notes (i.e., disregard only sources with *ppErrBits* flags greater than 255), but we checked that setting the flag threshold to 255 (or even down to 16) would result in too many sources with peculiar (and likely spurious) NIR colors, and therefore false positives in our selection (Sect. 3.2).

Moreover, filtering by magnitude errors did not improve the selection, since many suspicious flagged sources are characterized by very small formal errors. After removing VVV sources with all three flags *jppErrBits* > 0, *hppErrBits* > 0, and *kspErrBits* > 0, we obtain a final number of 2663602 clean VVV sources, that is approximately one-third of the initial catalog. Such a strong filtering likely excludes many thousand sources with only minor photometric inaccuracies (along with those with major accuracy problems) and therefore this step introduces a significant incompleteness in the VVV source catalog (with little magnitude dependence), probably by more than a factor of two. However, we checked that this does not introduce a spatial-dependent bias, which would be most harmful in our context. The limiting magnitudes for the VVV bands are derived from the histograms in Fig. 3 (bottom panels), as $J = 17.7$, $H = 16.8$, and $K_s = 16.2$, respectively, for sources with magnitude errors less than 0.1 mag. The same panels also show the magnitude distributions of discarded VVV sources: the discarded/good source number ratio increases towards the bright magnitudes, as is typical of systematic errors and the opposite to problems caused by low signal-to-noise ratio (S/N); also the detailed shapes of their distributions, especially that in the K band, suggest that these magnitudes are not very reliable and are better ignored.

Figure 3 also shows the bright limits for the VVV catalog, at $J \sim 14$, $H \sim 13$ and $K_s \sim 12$. Many Sco OB1 members, not only of OB types, are expected to be brighter than these limits. Therefore, we need to complete the VVV NIR dataset above its bright limit for a proper study of Sco OB1 low-mass stars. The most natural choice for this magnitude range is the 2MASS catalog (Cutri et al. 2003), complete approximately down to $J \sim 15$, $H \sim 14$ and $K_s \sim 13.8$, once we require magnitude errors less than 0.1 mag. We disregarded individual 2MASS magnitudes in the presence of at least one of: flag *ph_qual* equal to "E", "F", "U", or "X"; flag *rd_flg* outside the range [1–3]; nonzero *cc_flg* flag; flag *bl_flg* different from 1. This choice is more conservative than that adopted in some previous works (e.g., Damiani et al. 2006b, where we kept sources with confusion flag *cc_flg*="*c*"), and undoubtedly misses some real sources in dense regions[1]. However, since our present approach relies on accurate optical and NIR colors, we opted for the most conservative filtering, both on 2MASS and VVV data. There are 717232 clean 2MASS sources in the studied region.

We assembled a combined NIR catalog by positionally matching the VVV and 2MASS catalogs using a maximum distance of 0.2 arcsec. This yielded 118612 sources common to both 2MASS and VVV, and 3262222 unique NIR sources (the intersection and union of the two catalogs, respectively). The common magnitude range between 2MASS and VVV in each of the J, H, and K bands enabled us to calibrate the VVV photometry in the 2MASS system (see Appendix A). For sources detected in both datasets we selected the 2MASS magnitudes, to avoid an excessive number of missing values because of *ppErrBits* flagged entries in the VVV dataset. We examine in detail the spatial completeness of the combined NIR catalog in Sect. 4.

Using this combined NIR catalog and the VPHAS+ catalog we finally produced an optical-NIR catalog, by positionally matching sources within 0.2 arcsec. The total number of entries in this optical-NIR catalog is 4570242 (the union of input catalogs, including unmatched entries), while the number of stars detected in both the optical and the NIR is 706302 (intersection of input catalogs); see Fig. 4.

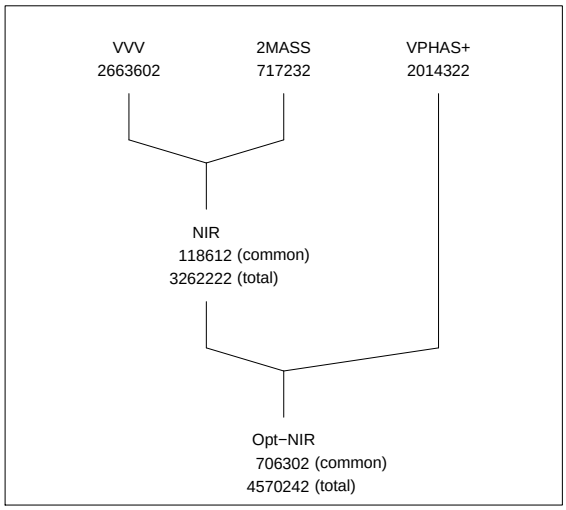

Fig. 4. Number of stars in each input catalog after cleaning, and construction of NIR and optical-NIR catalogs after source matching. Labels "common" and "total" refer to the intersection and union of input catalogs, respectively.

The Glimpse Source catalog (I + II + 3D, Spitzer Science Center 2009, available from CDS, Strasbourg) contains 719188 IR sources in our spatial region. Of these, we consider the subset (52740 sources) having magnitude errors less than 0.07 mag in each of the [3.6], [4.5], [5.8], and [8.0] bands.

2.2. X-ray data analysis

Besides the deep *Chandra* X-ray data on NGC 6231 presented in Damiani et al. (2016), we used the *Chandra* archive data on IRAS 16562-3959. This observation, made with the ACIS-I detector, was split in three pointings (ObsIDs 14537, 17691, and 16658; exposure times 5017 s, 40066 s, and 38576 s, respectively; PI: P. Hofner), nearly co-pointed and with total exposure time 83659 s. We have detected sources in the three pointings (co-added) using our detection code PWDetect (Damiani et al. 1997a,b), which is capable of dealing with combined *Chandra* datasets (see, e.g., our study of NGC 2516, Damiani et al. 2003). The chosen detection threshold corresponds approximately to one spurious detection in the FOV. We found 384 point sources in the IRAS 16562-3959 combined dataset, as listed in Table B.1. The spatial distribution of these sources and their connection with stars detected at other wavelengths are discussed in Sect. 4.

Relevant X-ray data on Sco OB1 are also found in the XMM-Newton archive, in addition to those on NGC 6231 published by Sana et al. (2006). We consider the XMM-Newton observation of the Wolf-Rayet star WR 79a (ObsID 0602020101, exposure 36080 s, PI: S. Skinner), which also covers part of Tr 24. We used our code PWXDetect (i.e., the version optimized for XMM-Newton data) to detect sources in the combined images from the three detectors in the EPIC camera (*pn*, MOS1, and MOS2). This code version was already used in previous cluster studies, for example, Sciortino et al. (2001). In this way, we detected 195 X-ray sources, listed in Table B.2, and discussed in Sect. 4.

[1] In practice, this has some consequences for this study only in the inner parts of NGC 6231.

3. Techniques for selection of young stars

In this section we discuss the various methods we use to select candidate PMS stars. We first present our method to photometrically select M stars, and the reasons why this is especially useful when applied to PMS stars. Then, other widely used photometric methods, such as those based on Hα, IR and UV excess emission, are also used to establish reference PMS star samples for the same sky region, which help us to test the effectiveness and reliability of our selection of M-type PMS stars.

3.1. M stars

Our method for identification of M stars in a star-formation region is based on a few key properties of these stars. First, it is commonly accepted that, during PMS evolution, stars contract toward the MS; despite significantly different details between various sets of model evolutionary tracks (such as Baraffe et al. 2015 – BHAC, or Siess et al. 2000), there is consensus on the fact that, among all spectral types, M-type stars (with masses in the range 0.1–0.5 $M_{\odot}$) show the largest luminosity excursion between an age of 1 Myr and their arrival on the zero-age main sequence. BHAC predict a difference of 3.3 magnitudes for a 0.5 $M_{\odot}$ star (i.e., a factor of 21 in $L_{\rm bol}$), and a difference of 5.0 magnitudes for a 0.1 $M_{\odot}$ star (a factor of 100 in $L_{\rm bol}$). For comparison, a 1 $M_{\odot}$ star evolves by only 1.36 magnitudes (a factor of 3.5 in $L_{\rm bol}$). Therefore, for a given limiting magnitude, a 1 Myr old 0.5 $M_{\odot}$ (0.1 $M_{\odot}$) star will be detectable until a distance 4.6 (10) times larger than a ZAMS star of the same mass. If a cluster of M-type PMS stars is present in a given sky region, it becomes prominent with respect to the field M dwarfs, detected only across a much smaller volume.

The second relevant property of M stars is that their spectral energy distributions are shaped in such a way that temperature and reddening become non-degenerate using suitable pairs of optical and NIR colors, as we discuss in detail below. The temperature-reddening degeneracy is instead rather ubiquitous for all hotter stars, and is ultimately responsible for a large fraction of non-member contamination in photometrically selected samples of members of a star-formation region.

We examined quantitatively the applicability of this selection method, for the VPHAS+ and VVV magnitude limits (Fig. 3). We considered isochrones from Siess et al. (2000) at different ages up to the ZAMS, converted to the VPHAS+ photometric system according to the prescriptions given in Drew et al. (2014). These isochrones, together with the above magnitude limits, were used to predict the maximum distance $\mathrm{d}_{X}^{\max}$ for detection of a star of given mass and age in each individual photometric band; for example, X. The maximum distance $\mathrm{d}_{XYZ}^{\max}$ for simultaneous detection in a given set of bands XYZ, for a star to be placed in the $(X-Y, Y-Z)$ color-color diagram, is equal to the minimum value among the limiting distances for the respective bands: $\mathrm{d}_{XYZ}^{\max} = \min(d_X^{\max}, d_Y^{\max}, d_Z^{\max})$. We also computed $\mathrm{d}_{XYZ}^{\max}$ for non-zero extinction of $A_V = 0, 1, 2, 3$ mag, which gave (obviously) gradually decreasing distances $\mathrm{d}_{XYZ}^{\max}$ toward the higher extinction values. These results are shown graphically in Fig. 5 for the band combinations (g, r, i), (r, i, J), and (r, i, H). The reason behind these choices of bands is discussed below. A fourth plot uses again the (r, i, J) bands, but this time together with the BHAC isochrone set to permit evaluation of the importance of model-related uncertainties (a comparison involving the (r, i, H) bands gives a similar result). The distance of NGC 6231 is shown as a reference. These diagrams, henceforth referred to as mass-distance-age (MDA) diagrams, are of the greatest importance for all the following development, and deserve a detailed analysis.

The (g, r, i) MDA diagram of Fig. 5a shows that with the available VPHAS+ data we are able to detect M stars at the distance of NGC 6231 and extinction $A_V = 1$ mag, down to a mass ~0.3 $M_{\odot}$, simultaneously in g, r, and i. Down to the same mass limit, MS M dwarfs are detected only up to ~600 pc, or a space volume 15 times smaller. The use of the g band might be a limiting factor for PMS stars, if they are found in obscured regions or dusty local environments; therefore, we examined the (r, i, J) MDA diagram, also shown in Fig. 5b. Here the distance between curves at different A_V values is reduced, as expected since the bands used are redder and less affected by extinction. For the NGC 6231 distance and $A_V = 1$ we detect stars down to a minimum mass of ~0.25 $M_{\odot}$, which rises only slightly to ~0.28 $M_{\odot}$ for $A_V = 2$. The limits obtained (Fig. 5c) using the H band in place of J are almost the same. Finally, using BHAC instead of Siess et al. (2000) models changes only small details in these predictions, as can be seen from comparing the two MDA diagrams in the right-hand panels. At 10 Myr, the intrinsic luminosity of PMS M stars diminishes, and with it also the contrast with the field M dwarfs; however, the average extinction is also often lower at this age with respect to 1 Myr, so the two effects partially compensate: a 10 Myr, $A_V = 0$ star at the NGC 6231 distance is detected in gri down to a mass ~0.4 $M_{\odot}$, and in riJ down to ~0.3 $M_{\odot}$.

The mere detection of M stars ensured by the above discussion, against a very crowded background of stars, would be of little use if not accompanied by a recipe to discriminate M stars from all other, hotter stars. This is possible since temperature and reddening are non-degenerate here, as mentioned before, and shown in detail below.

Our ability to select stars of M type using the available photometric data is demonstrated from the color-color diagrams in Fig. 6a, b, c, where both theoretical isochrones and observational data from our Sco OB1 optical-NIR catalog are shown. Each of these diagrams uses a combination of three photometric bands, corresponding to one of the MDA diagrams in Fig. 5. The vast majority of stars follow a linear locus, parallel to the reddening vector. Above that, a small number of stars deviate from that locus in each diagram. The isochrones and evolutionary tracks shown in the figure indicate that these deviant stars have colors corresponding to little-reddened M stars with masses $\leq$0.5 $M_{\odot}$, irrespective of their age between 1 Myr and ZAMS age. More massive stars instead show degenerate temperatures and reddening in these diagrams. We have therefore set fiducial limits for discrimination between the M stars and hotter stars, illustrated by the dashed lines in the figure. This was done in a rather conservative way, to minimize the number of false positives, or spuriously selected hotter stars. Only stars with errors less than 0.1 mag on each color are shown in the respective diagrams. In panel a of Fig. 6 the shape of the M-star locus appears different (more vertical) from that of the model locus. This, however, may easily be related to a selection effect: the more massive M stars (~0.5 $M_{\odot}$) are also relatively brighter, and detectable in the g band also in the presence of moderate reddening. Instead, the less massive stars (~0.2 $M_{\odot}$) near the top of the group are much fainter (and probably more spatially dense), and detectable in g only at low reddening. In general, comparison between panels a and b shows that M stars detected in the g band are in general less reddened than those detected in the J band, as expected.

At colors $g - r \geq 3$, another loose group of stars can be seen in the $(g-r, r-i)$ diagram of Fig. 6a above the M-star limit: these are stars sharing their intrinsic colors with M dwarfs, however at

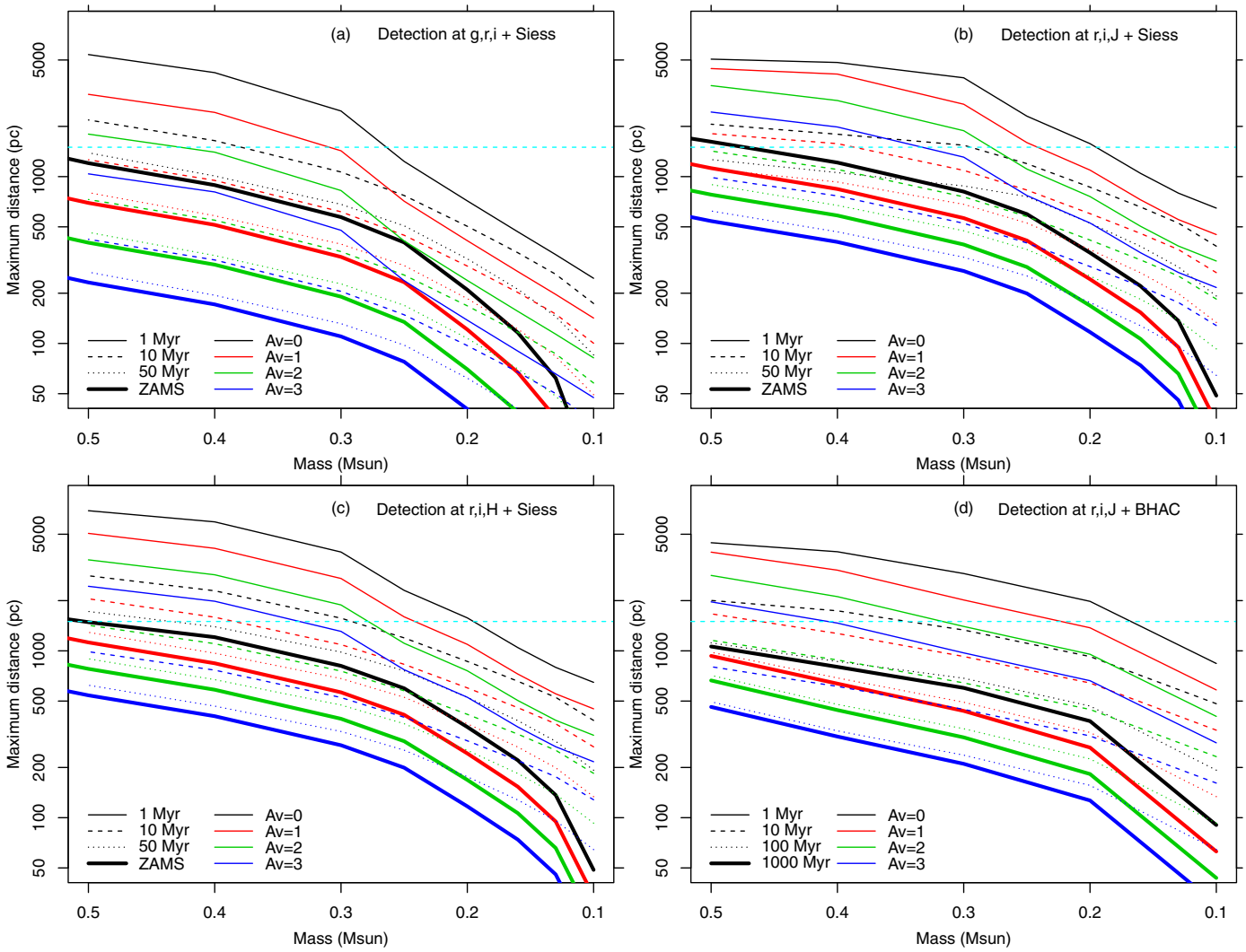

Fig. 5. Mass-distance-age (MDA) diagrams: maximum distances d^{max}_{XYZ} for simultaneous detection in three bands, using completeness limits from Fig. 3, and PMS evolutionary tracks from Siess et al. (2000) or BHAC, as indicated. The two *right panels* permit evaluation of the model-dependent uncertainties in the maximum distances. The cyan horizontal dashed lines indicate the distance of the NGC 6231 cluster.

much larger reddening. It is natural to identify them with distant M giants, which are so rare in terms of their absolute volume density that they are found predominantly at large distances (and reddening). This assumption is confirmed by their high observed brightness (median $i = 15.9$, compared to $i = 18.0$ for the M dwarfs), despite their larger reddening. These groups of M giants are also clearly evident in the $(i - J, r - i)$ and $(i - H, r - i)$ diagrams of Fig. 6b,c, and comprise the highest-reddening stars found in the latter diagrams. The importance of studying the background M-giant population in relation to the low-mass PMS population in Sco OB1 becomes clear in Sect. 4, below.

Therefore, we define as $M_{\rm gri}$ stars those selected using

$$(r - i) > 0.45 + 0.48\ (g - r) \quad (1)$$

(i.e., above the dashed line in Fig. 6a) and also $1.5 < (g - r) < 2.5$ to discriminate from high-reddening M giants. Similarly, $M_{\rm riJ}$ stars are defined as

$$(r - i) > 0.3 + 0.6\ (i - J), \quad (2)$$

and $1.4 < (i - J) < 3.0$. Also, $M_{\rm riH}$ stars are defined as

$$(r - i) > 0.25 + 0.45\ (i - H), \quad (3)$$

and $2 < (i - H) < 3.5$. The M giants are defined as: $gM_{\rm gri}$ from Eq. (1) and $(g - r) > 2.5$; $gM_{\rm riJ}$ from Eq. (2) and $(i - J) > 3.5$; and $gM_{\rm riH}$ from Eq. (3) and $(i - H) > 3.5$. The numbers of M-type stars selected, by type, are 5367 $M_{\rm gri}$, 5133 $M_{\rm riJ}$, and 4190 $M_{\rm riH}$ stars, with considerable overlap among the three groups, for a total number of 10224 low-reddening M stars (reported in Table B.3). The corresponding numbers for reddened M giants are 647 $gM_{\rm gri}$, 977 $gM_{\rm riJ}$, and 1447 $gM_{\rm riH}$ stars (total number 1936 stars). The overlap between the $gM_{\rm riJ}$ and $gM_{\rm riH}$ samples is nearly complete, while only 167 stars are common to the $gM_{\rm gri}$ and $gM_{\rm riH}$ samples.

If strong local extinction is present (circumstellar rather than interstellar dust), typically near the youngest stars, its effect might be to move an M star into the "reddened giants" subsample. We discuss in Sect. 4.1 that this latter subsample does not show spatial clustering, which argues against local extinction as being relevant for a significant number of Sco OB1 M stars.

To summarize, we have defined regions in several color-color diagrams which permit us to effectively select samples of M stars; the PMS M-type members of a star-formation region in the 1–10 Myr age range, and over a wide interval of distances and extinction, are expected to outnumber the much closer field

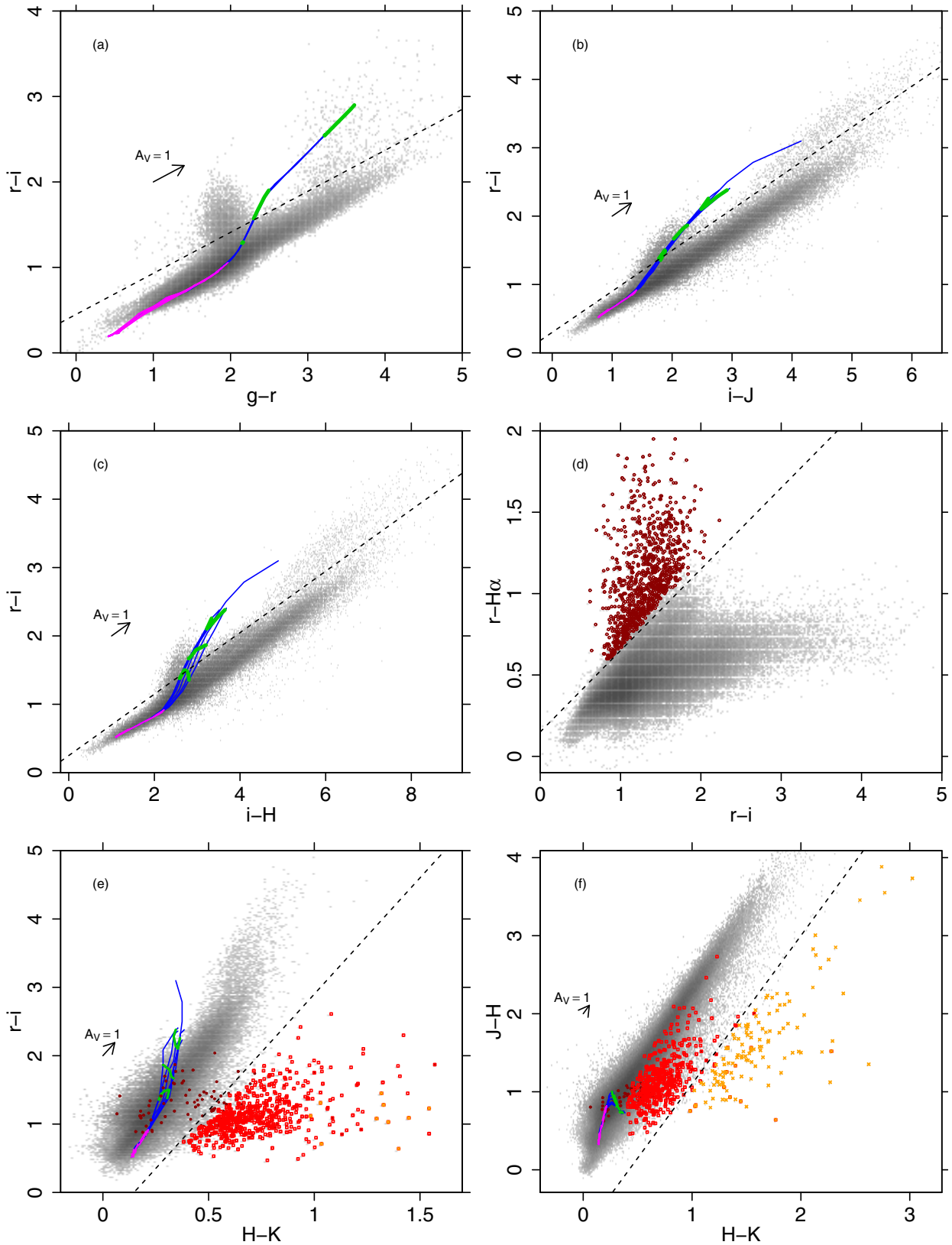

Fig. 6. Color-color diagrams used for selection of young stars. Each diagram is a two-dimensional histogram, with shades of gray indicating the density of datapoints. Only data with errors less than 0.1 mag on each pair of colors are shown. *Panels a–c*: M stars are found above the dashed lines. *Panel d*: strong Hα-emission stars are found above the dashed line (dark-red points). *Panels e–f*: IR-excess stars are found below the dashed lines (red squares: selected from $(H-K, r-i)$ diagram; orange crosses: selected from $(H-K, J-H)$ diagram; dark-red points from *panel d*). Representative reddening vectors are shown, except in *panel d* where reddening moves datapoints along curved trajectories. BHAC isochrones (evolutionary tracks) are shown with blue (green) lines for ages 1, 10, 50, and 10 000 Myr (masses of 0.1, 0.3, and 0.5 $M_\odot$), reddened as appropriate for NGC 6231 ($A_V = 1.5$). The location of stars with mass $M > 1\,M_\odot$ (all ages) is indicated with a magenta curve. In *panel a* only, Siess et al. (2000) isochrones and tracks are used, the BHAC set being unavailable for the g band.

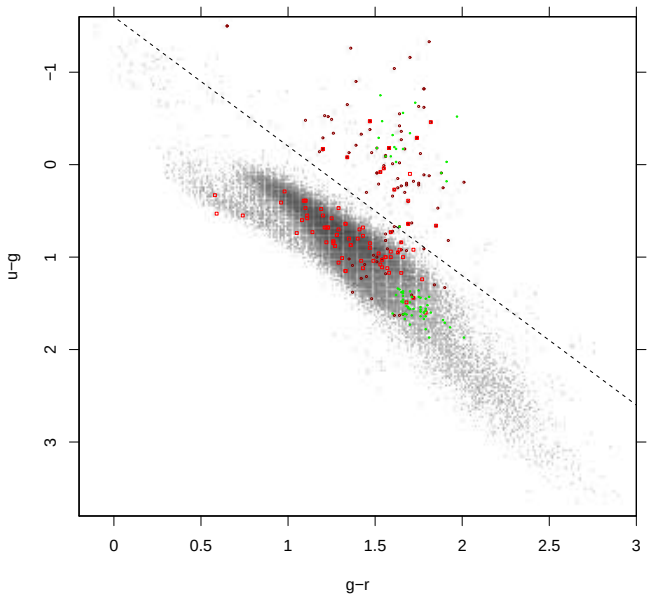

Fig. 7. A $(g-r, u-g)$ color-color diagram used for selection of UV-excess stars. Colored symbols as in Fig. 6, with the addition of green dots indicating M stars. UV-excess stars are found above the dashed line.

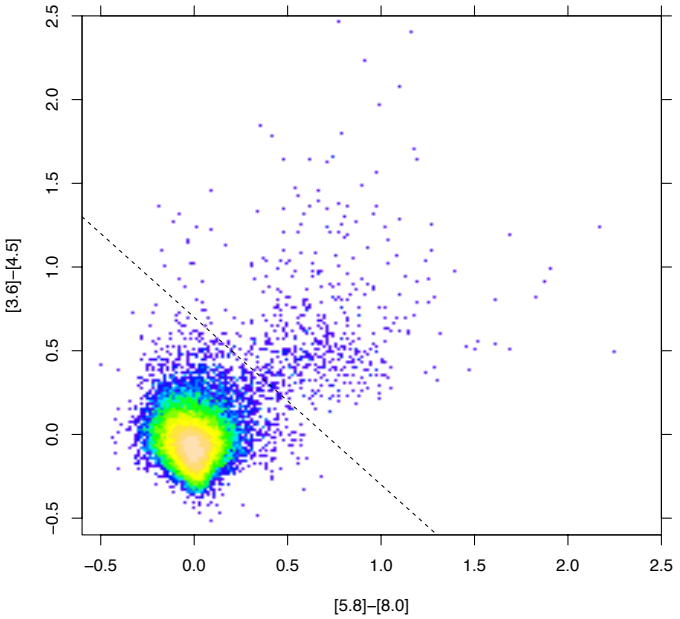

Fig. 8. *Spitzer* ([5.8]–[8.0], [3.6]–[4.5]) color-color diagram. Stars above the dashed line are YSO candidates.

M dwarfs in a magnitude-limited sample. The M stars selected in this way constitute therefore a good sample of candidate members of the star-formation region.

3.2. Hα emission, IR, and UV excesses

We considered also other diagnostics of PMS status in this study of Sco OB1. The first is photometric Hα excess, which is one of the fundamental products of the VPHAS+ survey. CTTSs are efficiently selected by using star positions in the $(r-i, r-H\alpha)$ diagram, as is done for example in Kalari et al. (2015) for the young cluster NGC 6530, or in our study of the NGC 7000 nebula (Damiani et al. 2017). We use a similar fiducial limit for the present VPHAS+ dataset in Sco OB1, shown in Fig. 6d:

$$(r-H\alpha) > 0.15 + 0.5\,(r-i). \quad (4)$$

Only stars 2σ above the fiducial limits were selected. This yielded 1082 Hα-excess stars in the entire region studied.

Class II members of a star-formation region are efficiently selected thanks to their NIR excess emission, best detected using the K band. It was argued in previous works (Damiani et al. 2006b, 2017; Guarcello et al. 2007, 2009; see also Strom et al. 1993; Eiroa & Casali 1995) that a mixed optical-NIR color-color diagram provides a more effective tool to select this type of PMS stars than an exclusively NIR-based diagram such as $(H-K, J-H)$. Therefore, we consider here the $(H-K, r-i)$ diagram, shown in Fig. 6e. As above, only stars with color errors less than 0.1 mag are shown. We set a fiducial limit, parallel to the reddening vector, and selected all stars with redder $(H-K)$ colors (above 2σ significance) with respect to that limit:

$$(r-i) < -0.5 + 3.4\,(H-K), \quad (5)$$

which yielded 849 optical-NIR excess stars.

Figure 6f is instead the usual $(H-K, J-H)$ diagram, from which, using the fiducial limit shown, that is:

$$(J-H) < -0.8 + 1.9\,(H-K), \quad (6)$$

we select 233 NIR-excess stars. In the same diagram we show also the optical-NIR excess stars, which follow well the CTTS locus predicted by Meyer et al. (1997), at low IR excess levels. Therefore, our optical-NIR excess stars are unlikely to be dominated by spurious identifications between stars in the optical and IR catalogs.

Finally, we consider stars with a UV excess, found using the VPHAS+ u band. Ultraviolet emission in PMS stars is commonly associated with an accretion hot spot, where matter falling from the circumstellar disk hits the star surface and heats up. This type of measurement is often difficult both because the CCD sensitivity at these wavelengths is low, and because UV radiation is very sensitive to line-of-sight absorption toward the star. The $(g-r, u-g)$ diagram of Fig. 7 is a useful tool to find UV-excess stars. As above we set a fiducial limit, above which UV-excess stars are found (above 2σ significance), defined as

$$(u-g) < -1.6 + 1.4\,(g-r), \quad (7)$$

which yields 233 stars. Of them, 127 were already selected as Hα- or NIR-excess stars. On the other hand, 132 stars with Hα- or NIR excess and measured u magnitude (with error less than 0.1 mag) show no u-band excess.

Stars with Hα-emission, optical-NIR excess, or u-band excess are also reported in Table B.3.

3.3. IR-excess sources from Spitzer

Photometric data from the *Spitzer* space observatory are also very useful to select populations of Class II (or Class 0-I) stars, thanks to their longer-wavelengths bands. Glimpse observations cover most of the Sco OB1 region studied here, with the notable exception of NGC 6231 and immediate surroundings. Figure 8 is a ([5.8]–[8.0], [3.6]–[4.5]) color-color diagram, which is effective to select Class 0-I-II sources (Gutermuth et al. 2009). We use this diagram here only to provide (additional) evidence for youth of stars found across Sco OB1, and therefore here we are not interested in the fine details concerning the IR classification

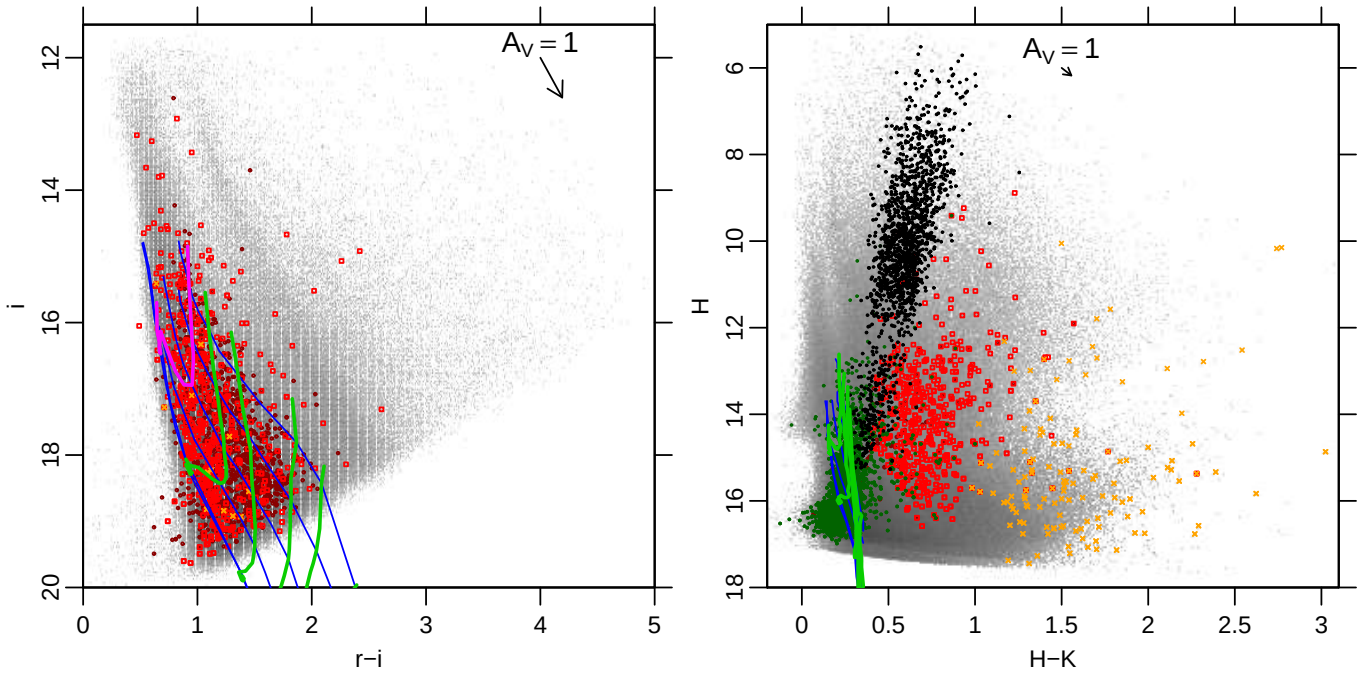

Fig. 9. Color-magnitude diagrams for all stars in the Sco OB1 region (*left panel*: $(i, r-i)$; *right panel*: $(H, H-K)$). Only data with errors less than 0.1 mag on colors and magnitudes are shown. Colored symbols, tracks, and isochrones as in Fig. 6. The magenta isochrone in the *left panel* corresponds to 1 $M_{\odot}$ stars. In the $(H, H-K)$ diagram, dark-green dots indicate all candidate M dwarf (or PMS) stars, while black dots are candidate M giants.

of sources. Accordingly, we defined a threshold in the ([5.8]–[8.0], [3.6]–[4.5]) plane above which most Class 0-I-II sources are expected to be found:

$$([3.6]-[4.5]) > 0.7-([5.8]-[8.0]); \quad (8)$$

other types of sources (e.g., extragalactic ones) are potentially found in the same region, but are unlikely to be numerous in these low-latitude fields, and if any, they are not expected to show spatial clustering, which is instead the case for PMS objects (see Sect. 4.1). The number of IR-excess objects selected in this way is 591.

3.4. Color-magnitude diagrams

The optical and NIR color-magnitude diagrams (CMD) using our combined optical-NIR catalog are shown in Fig. 9. Also shown are BHAC evolutionary tracks and isochrones, for the reddening and distance of NGC 6231. In the $(i, r-i)$ diagram, the Hα-excess stars do not form a narrow sequence, but are compatible with an age range between approximately 1 and 10 Myr, in agreement with the findings by Damiani et al. (2016) for NGC 6231. Many of the NIR-excess stars in the same diagram lie in places suggesting older ages, contrary to expectations; however, we show in Sect. 4 that the majority of these stars in our region belong to a diffuse galactic-plane population, not to Sco OB1.

The $(H, H-K)$ diagram in Fig. 9 (right panel) shows that the bulk of NIR sources in the region have very large extinction, of tens of magnitudes in V. There is a remarkable change in the source density near $H \sim 14$, which corresponds to the 2MASS-VVV transition: this is caused by incompleteness in the VVV catalog after our filtering, as explained in Sect. 2.1. The red $H-K$ colors of the NIR-excess stars do not necessarily correspond to high extinction, since they may largely be due to emission from circumstellar disks. The same figure also clearly shows the magnitude difference between our selected M dwarfs and giants: as mentioned, despite their large reddening, M giants are as a class distinctly brighter than the selected M dwarfs, with a magnitude gap around $H \sim 12.5$ between the two sets; a few stars in the "giant" subsample, fainter than that gap, might actually be dwarf stars.

4. Results: the Sco OB1 star-forming complex

4.1. Spatial morphology

The spatial distribution of the stellar samples selected using the methods described in Sect. 3 is shown in Fig. 10. The different panels permit us to understand in detail the spatial coverage of the VPHAS+ and VVV catalogs. The VPHAS+ data cover our region in a uniform manner, except for its western part. The tiles used in the VVV survey do not seamlessly cover the region, as is seen in the lower-right panel: lighter background corresponds to a lower NIR source density, where only 2MASS data are available. The missing areas, however, are a minor fraction and do not critically affect our results. In the first three panels, we also notice a reduced stellar density in the VPHAS+ catalog in the northeastern corner, corresponding to the region G345.45+1.50, which is characterized by both diffuse nebulosity and background obscuration. Moreover, the upper-left panel shows a clear lack of $M_{\rm gri}$ stars at $Dec < -42.1$, where g band data are still missing in VPHAS+ DR2.

The first three panels show separately the spatial distributions of $M_{\rm gri}$, $M_{\rm riJ}$ and $M_{\rm riH}$ stars, respectively. There is a nearly continuous distribution of these stars spanning an arc-like region from NGC 6231 up to G345.45+1.50, with densities in excess of neighboring fields. We have drawn with a large rectangle a reference field, where there is no indication of young stars associated to Sco OB1. Since the candidate PMS M stars are found

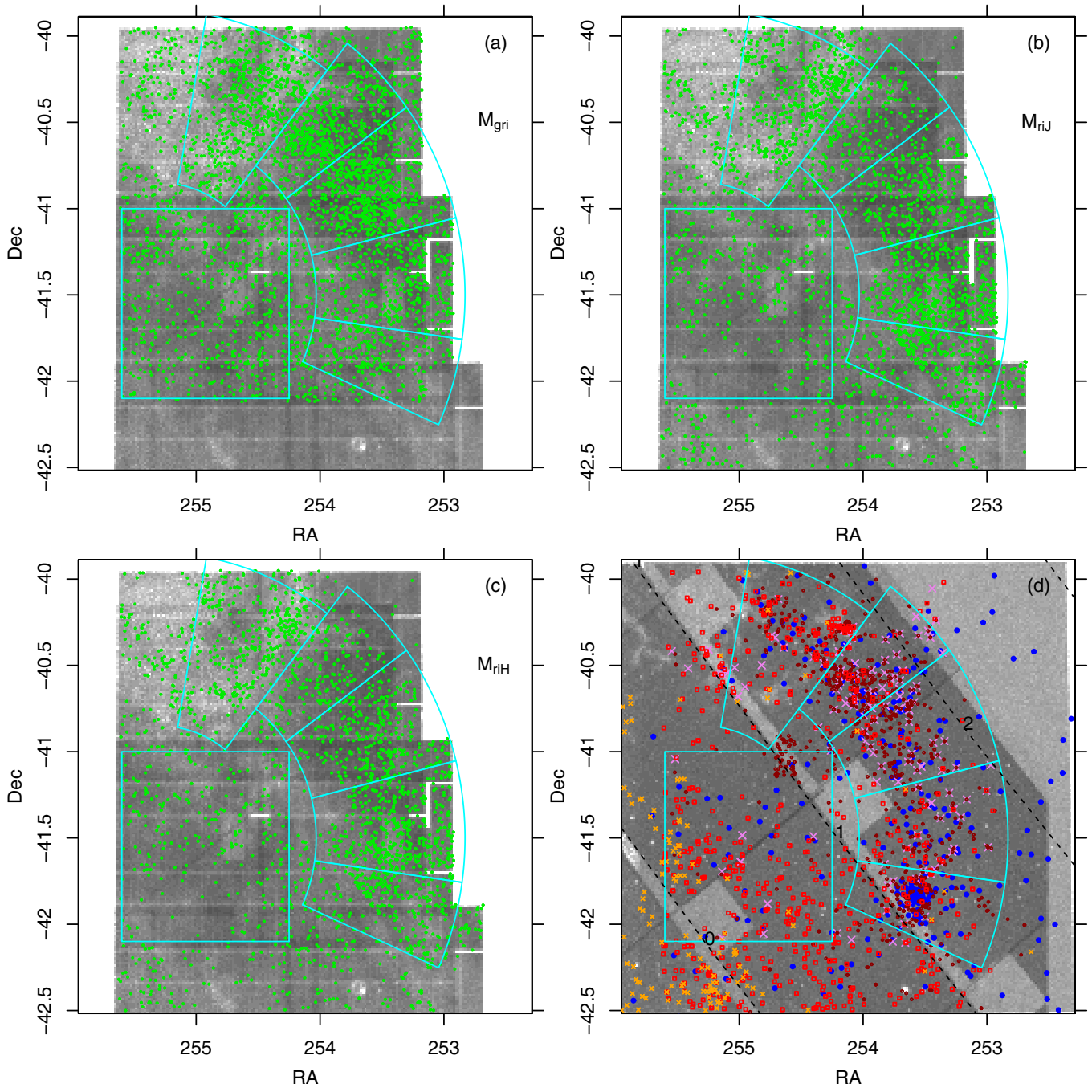

Fig. 10. Spatial distributions of star subsamples in Sco OB1. The background image is a two-dimensional density histogram of stars in VPHAS+ DR2 (and sources in our NIR catalog in the *bottom right panel*). *Top left panel*: M_{gri} stars (green) selected from Fig. 6a. *Top right panel*: M_{riJ} stars (green) from Fig. 6b. *Bottom left panel*: M_{riH} stars (green) from Fig. 6c. *Bottom right panel*: dark-red points, red squares and orange crosses are Hα-emission stars, and stars with optical-NIR and NIR excesses, respectively, as in Fig. 6; larger purple crosses are UV-excess stars from Fig. 7; big blue dots are O or B stars from SIMBAD. Oblique dashed black lines indicate constant galactic latitude b, as labeled. Spatial subregions of interest are indicated in all panels with cyan borders.

along a curved locus, we have instead selected five Sco OB1 subregions, also shown in the figure with sectors. The arguments presented in Sect. 3 indicate that the overdensities of M stars found in these sectors are made of good candidate members of this star-formation region. The lower-right panel shows instead the spatial distributions of Hα-emission stars, NIR- and UV-excess stars, and known OB stars: they describe a locus remarkably similar to the M stars, which strengthens our arguments on the M stars membership to Sco OB1. In the lower-left corner of the same panel, a large number of NIR-excess sources is found, with density increasing toward the galactic plane. These might be PMS stars or other dust-rich objects, but their spatial distribution suggests that they are unrelated to Sco OB1 and are not considered further. Also, a small group of Hα-emission stars near $(RA, Dec) = (254.6, -41)$ have no counterpart among NIR-excess or other young stars: they are also probably unrelated objects (or perhaps artifacts in the data).

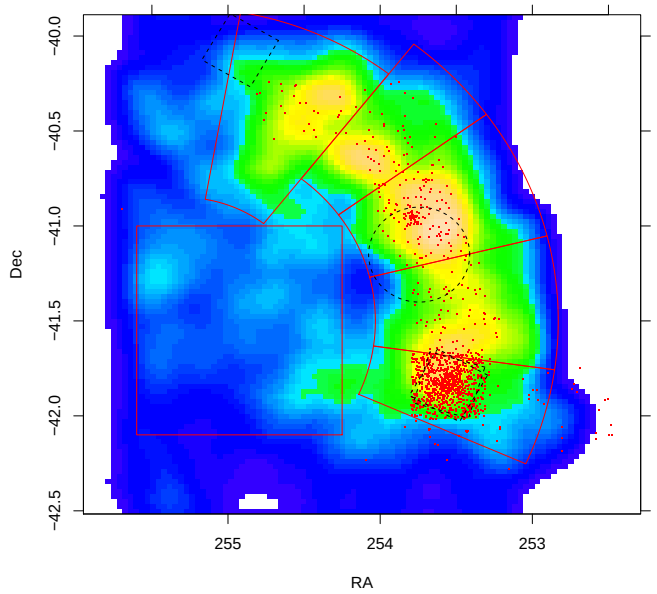

Fig. 11. Smoothed spatial distribution of all M stars (except for giants). The black dashed regions are the same *Chandra* and XMM-Newton FOVs as in Fig. 1. Red regions are the same as in Fig. 10. Red dots indicate all entries of type "stars in cluster" from the SIMBAD database.

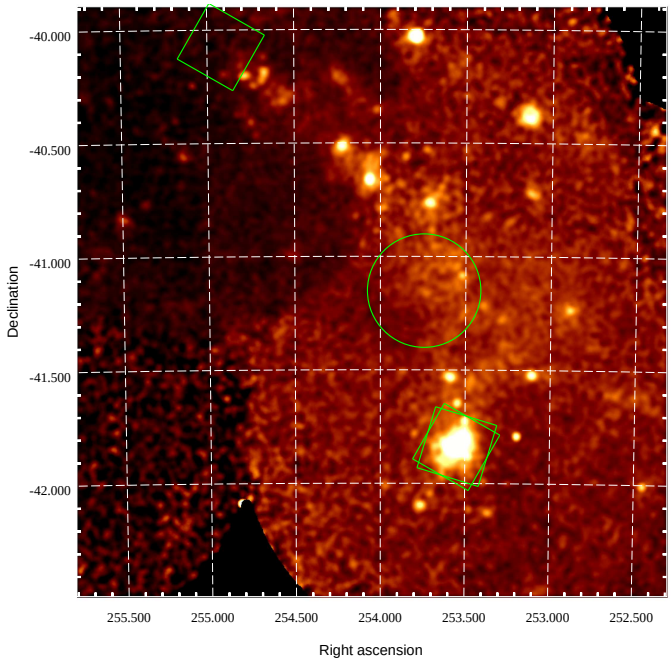

Fig. 12. ROSAT PSPC mosaic image of Sco OB1, Gaussian-smoothed with $\sigma = 85''$. The green regions are the same *Chandra* and XMM-Newton FOVs as in Fig. 1.

The comparison between panels a to c of Fig. 10 clearly shows that the $M_{\rm gri}$, $M_{\rm riJ}$, and $M_{\rm riH}$ star subsamples do not mutually coincide (e.g., the $M_{\rm gri}$ stars outnumber $M_{\rm riJ}$ stars in the second and third sector from top, but the reverse is seen in the fourth sector), which is explained by differences in the average properties of the stars (and their environments) among different subregions. This aspect is also discussed in Sect. 4.3 below. The differences among sectors 3–5 (counting from North to South) are likely explained as a result of decreasing foreground extinction from South to North (supported also by the results of Sect. 4.2), where smaller extinction favors more detections in the g band. The second sector from North does not fit into the sequence, however: here extinction is large, yet $M_{\rm gri}$ stars are more numerous than $M_{\rm riJ}$ stars. This subregion contains the bright nebula IC4628 and hosts a rich population of Hα-emission, NIR-excess, and UV-excess stars (Fig. 10d), all indicating a very young age. Therefore, the most likely explanation for the relative lack of $M_{\rm riJ}$ and $M_{\rm riH}$ stars here is that many M stars are still surrounded by moderately massive disks, whose emission causes their $i - J$ and $i - H$ colors to appear redder than a (reddened) photosphere, and shifted rightwards in the diagrams of Fig. 6b, c, by an amount sufficient to escape our $M_{\rm riJ}$ and $M_{\rm riH}$ selection criteria (though not necessarily large enough to cause these stars to be included in the NIR-excess sample).

A different representation of the spatial distribution of all M stars we selected (by any method) is provided by Fig. 11, smoothed using a 5-arcmin Gaussian kernel (a 3-arcmin kernel does not result in a significantly different map). Density variations shown by this map are not a byproduct of spatial incompleteness: for example, the reduced density found in the $M_{\rm riJ}$ and $M_{\rm riH}$ maps at $RA \sim 253.5$, above the main arc (Fig. 10b and c), might be ascribed to incompleteness in the NIR catalog, but a similar underdensity pattern is seen in the locally complete $M_{\rm gri}$ map (Fig. 10a); similarly, the $M_{\rm gri}$ map of Fig. 10a is obviously affected by incompleteness for $Dec < -42$ and is not useful to determine the southern bound of the arc-like region, but the $M_{\rm riJ}$ map of Fig. 10b shows that there is no M-star overdensity south of NGC 6231, so that the overall pattern shown by Fig. 11 can be considered reliable. The differences between subregions, discussed above, might to some extent affect the relative heights of the density peaks in Fig. 11, but much less their shapes, and since the $M_{\rm gri}$, $M_{\rm riJ}$, and $M_{\rm riH}$ selection methods tend to mutually compensate their respective weaknesses, this map is much more complete than any of the $M_{\rm gri}$, $M_{\rm riJ}$, or $M_{\rm riH}$ maps alone. The smoothed map of Fig. 11 shows clearly that the M star distribution is not actually continuous but shows four or five major clumps[2]. Each of the sectors we defined above corresponds to one such clump. From North to South, they correspond to: (1) the G345.45+1.50 region; (2) the IC4628 bright nebula, and the northern part of Tr 24; (3) the central part of Tr 24; (4) the southern part of Tr 24; and (5) the NGC 6231 cluster. The M star density outside of these five regions is much lower. The G345.45+1.50 region has the least uniform distribution of M stars, and also of NIR-excess sources (Fig. 10, lower-right panel); therefore we extended its sector radially toward the galactic plane.

We remark that NGC 6231, the densest and richest cluster in Sco OB1, does not correspond to the strongest peak in the M-star distribution in Fig. 11. While this is more quantitatively discussed in Sect. 4.3 below, we may already explain the reduced efficiency in M-star selection there from a combination of higher extinction and older age (Sects. 4.2 and 4.3), coupled to our very conservative filtering of input catalogs (Sect. 2.1) which rejects comparatively more stars in the densest regions, like the core of NGC 6231. On the other hand, the Hα-emission and IR-excess stars shown in Fig. 10d also include stars of types earlier than M, and are less affected.

[2] The densest part of the southernmost clump coincides with the NGC 6231 cluster, but the smoothed M-star distribution also shows a sort of tail to the north-west of NGC 6231, which we prefer to consider as a group distinct from the cluster.

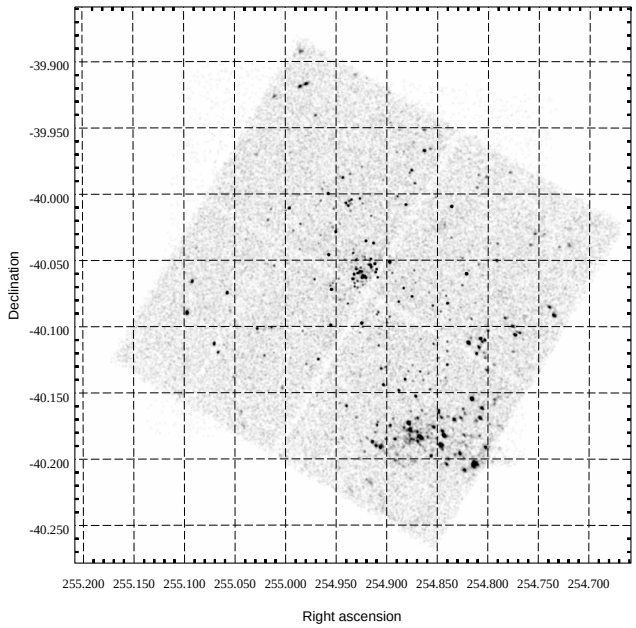

Fig. 13. *Chandra* ACIS-I image of the IRAS 16562-3959 region, slightly smoothed to emphasize point sources.

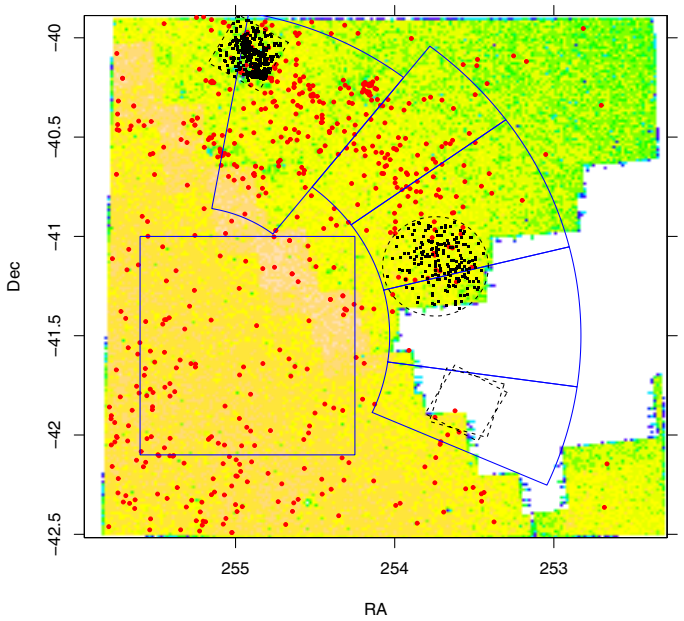

Fig. 14. Spatial-density 2D histogram (shades of color) for NIR sources in the *Spitzer* Glimpse catalog. Big red dots are *Spitzer* candidate YSOs. Small black dots are X-ray detections. *Chandra* and XMM-Newton X-ray FOVs (dashed black) are as in Fig. 1. Subregions (blue) as in Fig. 10.

Figure 11 also shows the distribution of all stars suspected to be members of some of the Sco OB1 clusters, from the literature studies mentioned in Sect. 1, which are of heterogeneous nature. Noteworthy is the small group of stars slightly offset to the East of the Tr 24 density peak: this group is named C 1651-408 in SIMBAD, and was also recently recovered in the study by Kuhn et al. (2017b; their Fig. 11). It is somewhat puzzling that this small cluster is not seen among Hα-emission or IR-excess stars (Fig. 10d), nor in X-rays (Fig. 12 below), and therefore increased extinction does not seem responsible for its non-detection as a distinct peak in the M-star sample; we conclude that this cluster is unlikely to be very young, despite lying very close to Tr 24 on the sky.

In Fig. 11 we also show the FOVs of existing X-ray *Chandra* and XMM-Newton observations. However, the entire Sco OB1 region was also observed nearly two decades ago using the ROSAT X-ray satellite. The detector used, the Position Sensitive Proportional Counter (PSPC), had neither the sensitivity nor the spatial resolution of *Chandra* or XMM-Newton, but with respect to them had a much larger FOV (2° diameter). The few existing PSPC pointings cover most of Sco OB1, unlike the *Chandra* and XMM-Newton data, and are shown in Fig. 12. Most of the diffuse background is caused by energetic particles, not cosmic X-rays, and varies between individual exposures. Nevertheless, local background structures (a few arcmin in size) are due to the unresolved X-ray emission from hundreds of faint sources; this diffuse emission, and a few individual, brightest X-ray sources including the entire cluster NGC 6231, describe an arc of enhanced emission very similar to the M stars, as expected if these are indeed a large population of X-ray bright low-mass PMS stars.

In the G345.45+1.50 region, the PSPC image shows enhanced emission inside the southwestern part of the corresponding *Chandra* ACIS-I FOV, and it is interesting to understand how the higher-quality *Chandra* data change the picture there. The ACIS-I image (analyzed in Sect. 2.2) is shown in Fig. 13: the unresolved PSPC emission is now resolved into a small cluster of more than 100 point X-ray sources; a distinct, smaller group of X-ray sources is instead found surrounding the target IRAS 16562-3959. These are most likely X-ray bright young stars inside the G345.45+1.50 H_{II} region. Interestingly, also the smoothed M-star distribution in Fig. 11 shows an enhanced M-star density in the southern part of the ACIS-I FOV. This is one more confirmation of the PMS nature of our selected M stars. Considering again the PSPC image, it also suggests an enhanced source density in the northwestern part of the XMM-Newton image (not shown for brevity); this is indeed the case, as shown by the distribution of XMM-Newton X-ray detections in Fig. 14. Therefore, the small clusters of X-ray sources seen in the available X-ray images are in full agreement with the picture that our M-star overdensities are indeed PMS members of Sco OB1.

Figure 14 also shows (as background) the spatial density of all *Spitzer* IR sources in the region, from the Glimpse catalog. Unfortunately the subregions Tr 24-South and NGC 6231 are not covered, which prevents a complete study. The YSOs selected from Fig. 8 are shown in Fig. 14: they are found in small groups especially in the G345.45+1.50 and IC4628 regions, similarly to the NIR objects from Fig. 10 and the X-ray sources in the IRAS 16562-3959 *Chandra* field of Fig. 13. This is fully consistent with the extreme youth of G345.45+1.50 and IC4628, while Tr 24 being older. The mentioned density enhancement of YSOs along the galactic plane (see Fig. 2) is also found among *Spitzer* sources. The *Spitzer* sources trace eminently galactic-disk objects, and their density declines rapidly for increasing b (i.e., toward northwest).

In order to more fully understand the environment where the Sco OB1 stars are found (and were likely born), we have computed a map of mean $(J - H)$, which is proportional to the average absorption toward objects in our NIR catalog. This is shown in Fig. 15, where green color corresponds to high-extinction regions (up to $A_V \sim 15$) and blue to lower extinction. Some stratification parallel to the galactic plane is evident, but also remarkable is that the G345.45+1.50 region

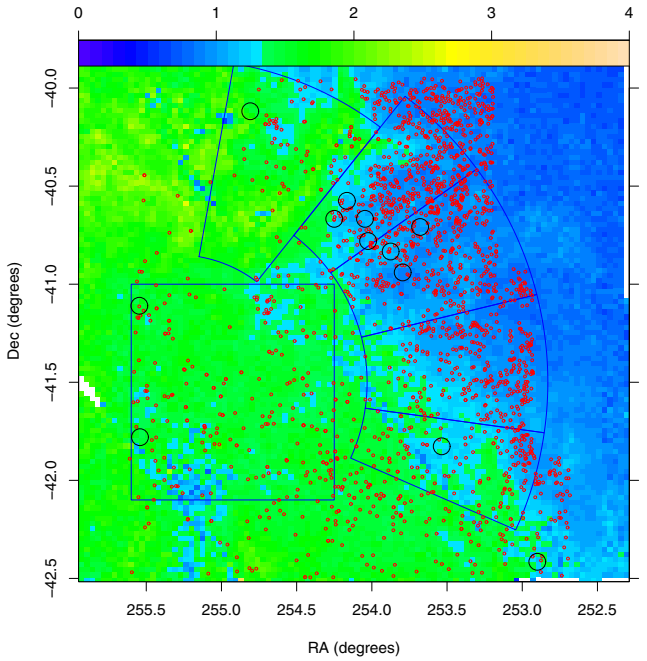

Fig. 15. Map of mean $(J - H)$ color (color scale shown in top axis). Subregions (blue) are as in Fig. 10. Red circles are high-reddening M stars (giants) from Fig. 6-a,b,c. Larger black circles indicate positions of known open clusters from SIMBAD.

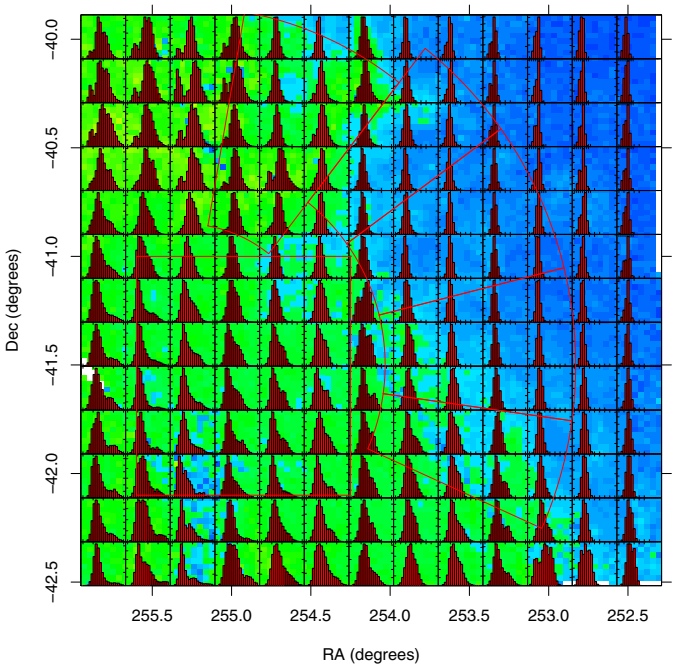

Fig. 16. Local distribution of reddening, from $(J - H)$ histograms (insets). The background image is the same as in Fig. 15. Subregions (red) are as in Fig. 10.

has higher extinction than regions at the same latitude b. Tr 24 is projected against lower-extinction regions, while NGC 6231 lies at intermediate extinction values, and was suggested to have itself excavated a local hole in the neighboring dust (Damiani et al. 2016; also partially seen in Fig. 15). The figure also shows the distribution of M giants: these populate densely the low-extinction regions, where they become observable up to large distances. Sco OB1 being located approximately 16° from the galactic center, these M giants belong probably to the galactic bulge. Therefore, their measured extinction provides a strong upper bound to the foreground dust column density toward the studied region. In the same figure we also show the positions of all known open clusters from SIMBAD: Apart from NGC 6231 and Tr 24, the other Sco OB1 clusters are very poorly known, small clusters (ESO 332-11, C 1652-405, ESO 332-13 in the IC4628 region; C 1651-408, C 1652-407, ESO 332-8 in the Tr 24 region). Interestingly, in the G345.45+1.50 region, the only IR-discovered cluster is found ([DBS2003] 115, Dutra et al. 2003), which is also coincident with the southernmost X-ray source cluster clearly seen in the *Chandra* image of Fig. 13, once again confirming its embedded nature and young age. The apparent spatial distribution of M giants, so tightly related to the total line-of-sight absorption, is markedly different from that of our candidate PMS M stars, which rules out that spatial overdensities of the latter are caused by holes in the dust column density.

Since absorbing dust is likely distributed over a wide range of distances along any given sightline, the average extinction obtained from $(J - H)$ provides only a rough description, being simply the first-order moment of the actual distribution in a given direction. A more detailed knowledge of the dust distribution is obtained by considering the histogram of $(J - H)$, in localized sky regions. The result of this approach can be seen in Fig. 16, where each histogram refers to a square spatial region of side 12′. Each histogram covers a $(J - H)$ range of $[0 - 4]$, corresponding to a maximum $A_V \sim 35$ magnitudes. The higher-latitude regions (with blue background) are confirmed as showing narrow $(J - H)$ distributions, with no tails at large values: this confirms that the total (not only the average) extinction in these directions is low enough ($A_V \leq 10$) to allow detection of bulge M giants. On the other hand, at lower latitudes, tails at high $(J - H)$ are regularly found. In the G345.45+1.50 region, the $(J - H)$ histogram is most complex, with two strong and well-separated peaks, and significant variations over adjacent spatial bins. The double peaks indicate a rapid rise of extinction with distance, caused by a thick dust layer or cloud, so that stars in its immediate foreground and background have markedly different $(J - H)$ colors, respectively, while $(J - H)$ variations are smoother along the rest of the line of sight. The Tr 24 regions (central, northern and southern) are among the most transparent; this suggests that no residual dust from the epoch of its formation has remained close to the cluster stars.

4.2. Extinction to M stars

As mentioned in Sect. 3, the colors of M stars are not degenerate with respect to extinction. This offers the opportunity for measuring extinction A_V for individual stars. The accuracy of A_V determinations depends on uncertainties both on the photometry itself and on the theoretical isochrones. At the level of precision of the available optical and NIR photometry, differences between the two isochrone sets used (Siess et al. (2000) and BHAC) are significant, and A_V derived from the $(g - r, r - i)$ diagram and Siess models (the BHAC models being unavailable for the g band) is only roughly correlated with A_V derived from the $(i - J, r - i)$ diagram and BHAC models. Since the BHAC models appear to better reproduce the observed datapoints in the $(i - J, r - i)$ diagram of Fig. 6, and also the CMD of NGC 6231 X-ray members in Damiani et al. (2016), we consider in the following only A_V obtained from the $(i - J, r - i)$ diagram and BHAC models.

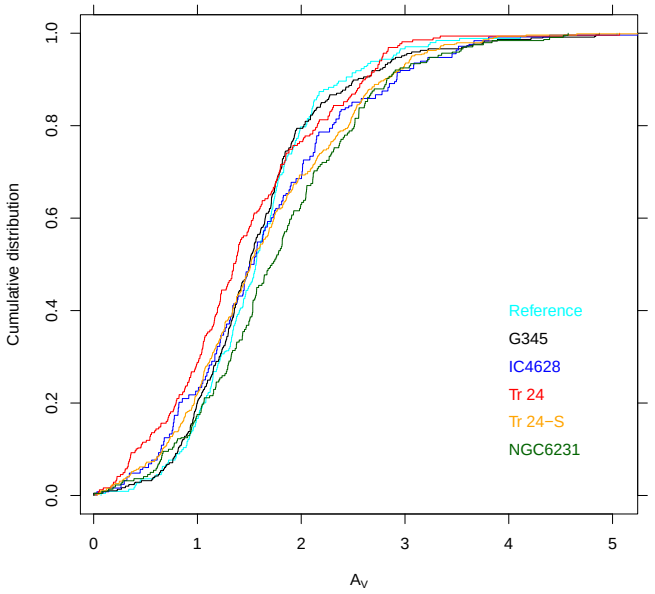

Fig. 17. Cumulative distribution of A_V for subregions, including the reference field.

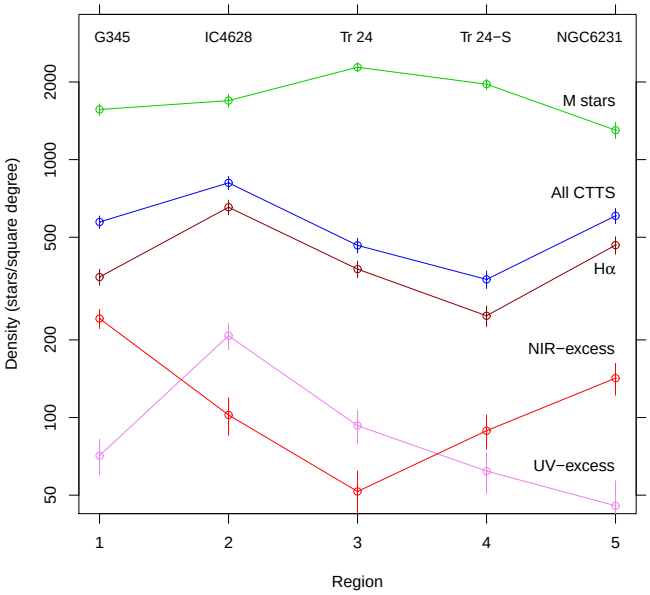

Fig. 18. Spatial density of M stars, Hα-excess, NIR-excess, and UV-excess stars for the different regions.

Figure 17 shows cumulative A_V distributions for M stars (not giants) in each of the five Sco OB1 subregions (and reference region) defined above. Values of $A_V < 0$ were reset to zero when compatible with zero within errors. Stars in NGC 6231 are characterized by the highest A_V distribution, which may be related to its relatively low latitude b compared to the other subregions. Schild et al. (1971) and Neckel & Klare (1980) find that most of the extinction toward this cluster arises much closer to us along the line of sight. Therefore, the enhanced A_V toward this cluster does not necessarily imply that its neighborhood contains more dust than the other subregions. On the other hand, the G345.45+1.50 region, which is an active star-forming region as summarized in Sect. 1, and contains a thick dust cloud as seen from Fig. 16, has only M stars with relatively low A_V: these are probably found on its near side, closer to us than the dusty layers. We compared the A_V distributions pairwise between subregions using Kolmogorov-Smirnov tests. All visual differences in Fig. 17 are statistically very significant: for example, the NGC 6231 extinction is larger than that in the neighboring Tr 24-S region at the 99.97% confidence level. This latter, on the other hand, is larger than that in the central Tr 24 region at the 99.9% level. The central Tr 24 region has the lowest extinction, both foreground as seen from Fig. 17, and in its background as seen from Fig. 16.

4.3. Member statistics and ages of M stars

While we argued in Sect. 4.1 above the qualitative evidence that most selected M stars are indeed tracing the low-mass population of Sco OB1, we here discuss their quantitative statistics, and compare them with member samples found using other techniques. Table 1 (and Fig. 18) reports the number of M stars (by type and cumulatively) in each subregion, together with their estimated net number, obtained by subtracting the (area-scaled) number of stars in the reference field. Also given are the M-star net mean surface densities, and the estimated fractions f_C of non-member contaminants, together with the numbers of member stars selected using the other techniques discussed in Sect. 3. Although the absolute numbers of Hα-emission and IR-excess stars in NGC 6231 are among the largest of all subregions, they become the smallest in relative terms, once they are scaled to the respective numbers of OB stars. This is discussed in more detail below in connection with relative cluster ages. Contaminant fractions f_C are computed using the detected M-star population in the Reference field, with an area scaling factor for each sector. As discussed in Sect. 3.1, these contaminants are mostly MS M stars, with a negligible fraction of low-reddening giants. This procedure relies on the assumption that the distribution of absorbing dust with distance from us is approximately the same in the Reference field and in the Sco OB1 subregions, which is to a first approximation true from consideration of Fig. 17 (as far as only M stars are concerned). We note from Table 1 that the level of contamination is significant ($f_C \sim 0.37$–0.51), and therefore the membership of any particular star in our sample can only be assessed using additional data; however, the (relative) error on the net number of stars is small enough to imply a highly statistically significant population of Sco OB1 members, in any of the considered subregions.

Unlike M stars, there are virtually no Hα-emission nor IR-excess stars immediately outside Sco OB1 subregions. The Reference field does contain many of them, but it was argued in Sect. 4.1 that they are populations of stars lying at very low galactic latitudes, not extending to the slightly higher latitude of Sco OB1. The contamination of Hα-emission and IR-excess Sco OB1 stars can therefore be considered negligible.

We note that there are large differences in the $M_{\rm gri}/M_{\rm riJ}$ number ratio between different subregions, which might be at least partially related to differences in foreground extinction (the blue g band being more affected than the J NIR band), and by consequence different minimum detectable stellar mass, from the MDA diagrams of Fig. 5. This latter figure, however, predicts that the minimum detectable mass using the (r, i, J) bands is always lower (using this particular photometric dataset) than the minimum detectable mass using the (g, r, i) bands; therefore, the number of $M_{\rm gri}$ stars should always be lower than that of $M_{\rm riJ}$ stars. This does not appear to be the case in the IC4628 or Tr 24 subregions, where $M_{\rm gri}$ stars evidently outnumber $M_{\rm riJ}$ stars. This peculiarity may be explained by recalling that the adopted

Table 1. M stars and young objects in Sco OB1 subregions.

N	Region name	Area	$M_{\rm gri}$	$M_{\rm riJ}$	$M_{\rm riH}$	$M_{\rm tot}$	Net	Net Err.	Density	Density Err.	f_C	Hα	NIR	UV	OB
0	Reference	1.11	939	604	458	1502	0.00	54.81	0.0	49.3	1.00	65	221	12	
1	G345	0.56	969	856	668	1638	879.04	44.96	1564.1	80.0	0.46	197	136	40	8
2	IC4628	0.35	732	348	290	1071	595.82	34.95	1693.4	99.3	0.44	230	36	73	32
3	Tr 24	0.48	1056	697	625	1757	1103.63	45.18	2281.1	93.4	0.37	182	25	45	26
4	Tr 24-S	0.48	593	1015	837	1602	948.63	43.43	1960.8	89.8	0.41	120	43	30	22
5	NGC6231	0.35	340	598	480	933	457.82	32.91	1301.2	93.5	0.51	164	50	16	94

Notes. Column Area is the region area in square degrees. Column $M_{\rm tot}$ is the total number of M stars. Column Net reports the net number of M stars. Column Density is the net M-star density in units of stars/sq.deg.. Column f_C gives the number ratio between M non-members and all M stars in the given subregion. Columns Hα, NIR, UV, and OB report numbers of Hα emission, NIR-excess, UV-excess, and (net) OB stars, respectively.

filtering for the VVV data implied a (confusion-related) incompleteness by almost a factor of three in the NIR catalog (see Sect. 2). The numbers of $M_{\rm riJ}$ and $M_{\rm riH}$ stars found are therefore to be regarded as underestimates, by a factor up to approximately two. As mentioned in Sect. 4.1, circumstellar disk emission may also deplete the $M_{\rm riJ}$ and $M_{\rm riH}$ samples relative to the $M_{\rm gri}$ sample. The simultaneous use of several triplets of bands proves therefore useful in that they complement each other, such that incompleteness in the final selected population is reduced to a minimum.

The last column in Table 1 reports the number of OB stars minus the "diffuse" population estimated from their density in the Reference field (22.5 stars per square degree): as is immediately seen, the M-star statistics is much larger than the OB star statistics. This can hardly be considered surprising, if an ordinary IMF (e.g., that from Weidner et al. 2010) is assumed for the star-formation region. In Fig. 19 we show the density ratio between M and OB stars, which provides a consistency test between our results and a plausible IMF: this ratio varies however by a large factor, close to 20, among our subregions. This might reflect differences in the respective IMFs, but also differences in completeness among the stellar samples considered for the various regions. We first note that the ratio between M and OB stars in NGC 6231 is dramatically lower than anywhere else in Sco OB1. We can indeed expect that M stars are detected less efficiently in the inner parts of NGC 6231, where the density of bright stars is very large, and their diffuse glare raises the limiting magnitude locally. As already discussed above in Sect. 4.1, this causes our sample of M stars in NGC 6231 to be highly incomplete. Moreover, we determined above that NGC 6231 is significantly more extincted, by almost half a magnitude in V, than Tr 24, and this implies a higher minimum detectable mass among NGC 6231 M stars compared to Tr 24 (see the MDA diagrams in Fig. 5); this effect reduces the completeness of the M-star sample in NGC 6231 more than in Tr 24. If Tr 24 is also slightly younger than NGC 6231, as we argue below, our M-stars in Tr 24 will reach down to lower masses than in NGC 6231, with a steep increase in the detected M-star population: adopting the IMF from Weidner et al. (2010), the predicted number of cluster M stars doubles considering the mass interval 0.25–0.5 $M_\odot$ rather than 0.35–0.5 $M_\odot$. If Tr 24 is younger than NGC 6231, moreover, its stars in the mass range 2.5–3 $M_\odot$ might not have yet reached their ZAMS position as B stars, and therefore would not be counted among OB stars; this would further raise the M/OB star ratio there by up to 30%. Therefore, the proportions of both M and OB stars that are detected in a young cluster will depend on their age and extinction, in accordance with the MDA diagrams, even for a fixed, spatially uniform photometric sensitivity.

We estimated using the Weidner et al. (2010) IMF the expected range for the observed M/OB number ratio. Siess et al. (2000) predict that the latest-type B stars have a mass of ~3.5 $M_\odot$ at 2 Myr, and ~2.2 $M_\odot$ at 10 Myr, that is, in the range of ages expected for Sco OB1 clusters. The MDA diagrams of Fig. 5 predict that the lowest-mass stars we are able to detect using the available Sco-OB1 data have ~0.2 $M_\odot$, even assuming the most favorable (and unlikely) circumstances of an age less than 2 Myr and negligible reddening. The extreme values found for the M/OB ratio are then ~3.8 for a minimum M-star mass as high as 0.35 $M_\odot$ and an old age of 10 Myr, and ~20 for a minimum M-star mass as low as 0.2 $M_\odot$ and age of 2 Myr. These extremes are also shown as horizontal lines in Fig. 19. We note that the M/OB ratio in NGC 6231 falls well within this range; however, both Tr 24 regions are significantly richer of M stars than expected, by more than a factor of two and well above (statistical) errors. If true, then paradoxically this part of the OB association would form preferentially lower-mass stars. Of course, more detailed studies are needed to confirm this result. In the G345.45+1.50 region the M/OB ratio is highest, and far above predictions from the IMF: we may tentatively explain this since this region is very young, and some of its most massive members, like IRAS 16562-3959, are still in formation, thus decreasing the number of optically revealed OB stars. The lowest M/OB ratio in NGC 6231 is unlikely to be real, since as discussed above our M-star sample in this densest subregion is likely incomplete.

Here we examine if an age sequence can be identified among these subgroups. As explained in Sect. 1, G345.45+1.50 is surely a very young region (it contains masers, bright and dark nebulosity, and its stars show an irregular spatial distribution), while on the other hand at the opposite extreme NGC 6231 is much older (it contains no protostars or stars younger than 1 Myr, and has a relaxed morphology). The question is therefore if the ages of the other subgroups lie along an ordered sequence, of which G345.45+1.50 and NGC 6231 are the extremes.

Figure 18 shows that in proceeding from Tr 24 toward G345.45+1.50, the density of NIR-excess stars increases, as expected if an age sequence exists. However, both the Hα-emission and UV-excess stars decrease in density, contrary to expectations. This may be caused by locally increased Hα background in G345.45+1.50, and by circumstellar absorption near the youngest stars, which may prevent their detection in the Hα and u bands, respectively. As a result, no single indicator among Hα emission, NIR, or UV excess can be taken as a reliable indicator of youth here.

We instead consider collectively all PMS stars with NIR excess (Class II), Hα emission, or UV excess as CTTS (also

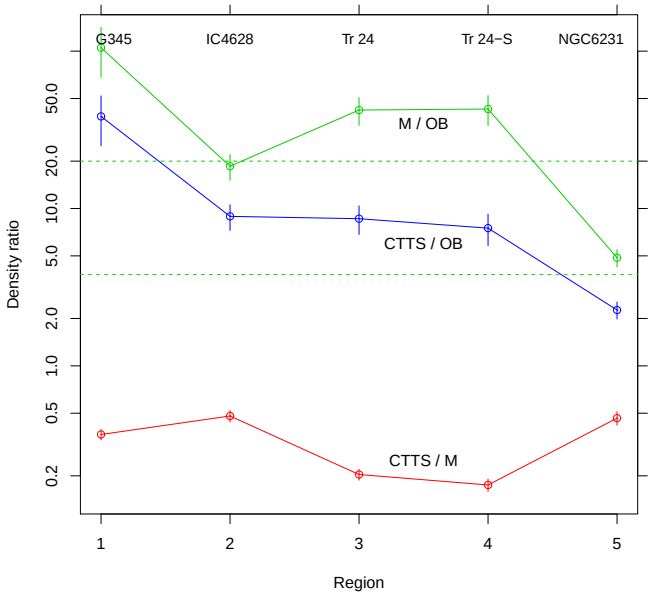

Fig. 19. Net stellar density ratios between M and OB stars, cumulative CTTS and OB stars, and CTTS and M stars, for each subregion. The green dashed lines indicate the maximum and minimum values expected for the M/OB number ratio.

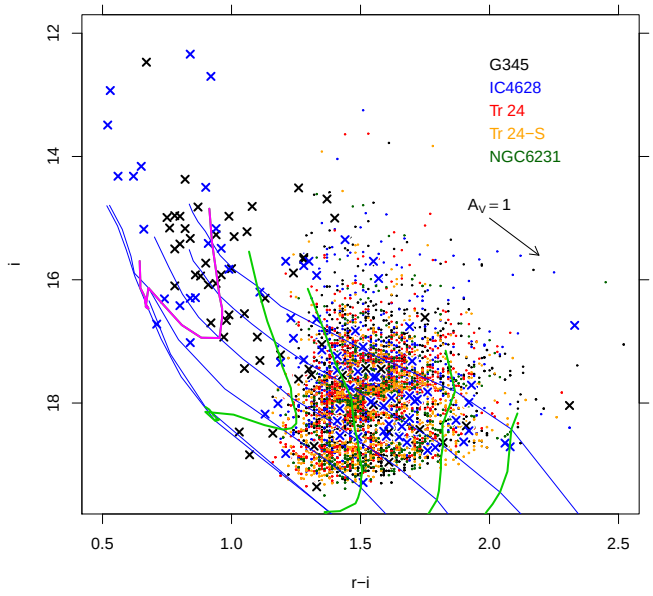

Fig. 20. The $(i, r-i)$ CMD of all M stars, color-coded by spatial region. Also shown are X-ray detections from XMM-Newton (black crosses) and *Chandra* (blue crosses). Tracks and isochrones as in Fig. 9.

shown in Fig. 18). The number ratio between CTTS and the total population in a subregion may be taken as a better indicator of its youth. We have computed density ratios between CTTS and M stars, and between CTTS and OB stars (see Fig. 19); Since as shown above the M/OB density ratio varies wildly between subregions, the CTTS/M and CTTS/OB ratios do not show the same trend across regions. The CTTS/M ratio does not seem to be a reliable indicator of age, being essentially the same in G345.45+1.50 and NGC 6231, which are of different age with high certainty. The CTTS/OB ratio, on the other hand, is fully consistent with our expectations of an increased proportion of CTTS stars in G345.45+1.50 compared to anywhere else in Sco OB1, and shows a regular monotonic increase from NGC 6231 to G345.45+1.50. This suggests a sequence of decreasing age, and therefore that star formation has progressed in a regular fashion from the oldest NGC 6231 region, through the intermediate age Tr 24 and up to the youngest region G345.45+1.50.

We have also tried to derive ages for the M stars directly from the optical CMD and BHAC model isochrones (Fig. 20). The M stars of all subregions are spread over a wide range of ages, which dominates over mean age differences between individual subregions. We show also the X-ray sources detected with *Chandra* (in the G345.45+1.50 region) and XMM-Newton (in Tr 24), which also do not follow narrow sequences, but are consistent with an age range between 1 and 10 Myr. A similarly large age spread was already found from the deep *Chandra* data on NGC 6231 (Damiani et al. 2016). As expected, the X-ray data select stars over a wide range of masses, often above 1 $M_\odot$.

5. Discussion

From all above results it seems very likely that NGC 6231, Tr 24, and the nebulous regions IC4628 and G345.45+1.50 are physically related and all belong to the same Sco OB1 star-formation region (or better, Sco OB1 star-formation complex), with each subregion corresponding to an episode of stellar formation along an ordered South-North sequence, spanning slightly more than 50 pc in total length.

We have recently determined the total mass of NGC 6231, based on a large catalog of more than 1600 members, as 4380 $M_\odot$ (Damiani et al. 2016)[3]. From Table 1 we derive that the total number of OB stars in Sco OB1 subregions 1–4 (88 stars) is 94% of the OB stars in NGC 6231. If total mass scales with the number of OB stars, we predict therefore a mass of 4120 $M_\odot$ for the G345.45+1.50, IC4628 and Tr 24 regions collectively, and a total stellar mass of 8500 $M_\odot$ for the entire Sco OB1 complex. If there is a real excess of M stars in Tr 24, as discussed above, the estimated mass would be significantly larger, since M stars in the mass range 0.2–0.5 $M_\odot$ constitute ~20% of the total mass, assuming the IMF from Weidner et al. (2010). Still, the above mass estimate of 8500 $M_\odot$ would make the Sco OB1 complex the tenth most massive star-formation region in the Galaxy, according to the Weidner et al. (2010) list.

NGC 6231 is both the oldest and most massive subregion in Sco OB1. Assuming an age of 5–7 Myr for NGC 6231 (Sung et al. 2013; Damiani et al. 2016; Kuhn et al. 2017a find a slightly younger median age of ~3.3 Myr) and 1 Myr for G345.45+1.50, the observed age sequence in Sco OB1 would suggest a star-formation episode every ~1 Myr, spaced by ~10 pc. If they were caused by some form of triggering, the perturbation was moving at about 10 km/s, close to the sound speed inside an H_{II} region. At earlier times, NGC 6231 undoubtedly created a bright H_{II} region, whose remains are still observable as the Gum 55 nebula, a weak Hα ring (5° in diameter) centered on NGC 6231 (Reipurth 2008). Why this wave of star formation proceeded only in one direction, and why it caused distinct episodes instead of a continuous stream of new stars, remains completely unclear. Also needing better clarification are the different age ranges found by Sung et al. (2013) between high- and low-mass stars in NGC 6231 (4–7 Myr and 1–7 Myr, respectively).

The different morphologies of the spatial distribution of PMS stars in the individual subregions are also remarkable.

[3] Kuhn et al. (2017a), using a slightly deeper catalog, derive a similar cluster mass of 3300–4200 $M_\odot$.

NGC 6231 has the most regular shape, with a (nearly) circular symmetry (Damiani et al. 2016; more detail about the cluster morphology is available from Kuhn et al. 2017b). At the opposite extreme, PMS stars in G345.45+1.50 are regrouped in small subclusters: two are seen in Fig. 13, and a few more in Fig. 10 (lower-right panel). Also in the IC4628 region PMS stars (especially those with Hα and NIR excess) tend to form small clumps. Tr 24 has a very wide spatial distribution, which was already found as remarkable by Seggewiss (1968), and somewhat anomalous by Perry et al. (1991). These latter authors argued that the existence of the Tr 24 cluster itself was questionable, on the basis of its atypical appearance, while our results clearly indicate that it exists, and has a large spatial size.

While dynamical processes have surely erased any signatures of its original spatial distribution, we may by analogy assume that at birth Tr 24 was a discrete collection of clumps of stars, like in the G345.45+1.50 and IC4628 regions (or, e.g., like the subgroups of PMS stars in the NGC 7000/IC 5070 complex; see Damiani et al. 2017). This would explain the lack of a definite center among its OB stars, which were regrouped by Seggewiss (1968) in three different subclusters. The more mobile M stars do instead define a clear center (Fig. 11). Alternative explanations, such as a rapid expansion after gas removal (in a shorter time than NGC 6231), seem less likely, since the relatively few OB stars in Tr 24 would have taken more time to disperse the surrounding cloud than the time taken by the NGC 6231 OB stars to disperse their own. Since little dust is found in the Tr 24 direction, and Tr 24 OB stars are comparatively few, this cluster probably formed in a lower-density environment compared to NGC 6231.

Containing less mass in a wider spatial region, Tr 24 is probably less bound than NGC 6231 (confirmation would require better kinematical data than available today). Therefore, it might be a good candidate as a cluster in the early dissolution phase (Lada & Lada 2003): as discussed in Sect. 1, most clusters are predicted not to survive after 10 Myr, but no clear observational evidence exists of the dissolution process itself. As PMS stars become more and more spread over large spatial regions, the chances of identifying them as a population decrease rapidly with decreasing density contrast with the field-star population. Our method for finding large numbers of low-mass PMS star candidates over large sky areas is therefore very promising for an observational study of this transitional phase of cluster evolution.

It is often stated, and confirmed by kinematical studies, that stars in a cluster share a common space motion, inherited from the parent molecular cloud. In the case of two clusters, such as NGC 6231 and Tr 24, which appear to have originated from the same cloud (they are also considered as a double cluster by Korkov & Orlov 2011) only a few million years one after the other, this may lead to a rapid collapse if the cloud was not rotating, since the two clusters would fall toward their common barycenter. Assuming no residual gas, and two clusters with the above-inferred masses and distances for NGC 6231 and Tr 24, respectively, collision would occur after ~17 Myr, of which the age of these clusters is an appreciable fraction. Since Tr 24 is so extended and NGC 6231 much more massive and compact, we would expect tidal tails to develop on both sides of Tr 24, toward and away from NGC 6231. Stars in the Tr 24-S region might in fact constitute one of these tails. Their distribution in Fig. 11 does not point directly toward NGC 6231, but is suggestive of rotation with respect to the inter-cluster axis. A rotating parent molecular cloud is more likely than a non-rotating one, and this might have prevented free fall of one cluster toward the other (which is also ruled out by the results from Laval 1972b, indicating expansion). A rotating cloud might also explain the curved shape of the whole Sco OB1 complex. Moreover, Laval (1972a) finds that gas in the North and South of Sco OB1 moves at different radial velocities. Applying Kepler's third law to two idealized point masses of the order of NGC 6231 and the rest of Sco OB1, with a semi-axis of 12 pc, and a barycenter not far from NGC 6231 itself, which contains nearly half the total mass of the complex, gives a rough estimate of a rotation period of 40 Myr. During the ~6 Myr since their formation, the system would have rotated by ~54°, which is close to the bending angle of the star distribution seen in Fig. 11.

Finally, we consider the youngest region comprising G345.45+1.50 and IC4628, which has a very different appearance in the mid-IR (Fig. 2) compared to the optical (Fig. 1). A better figure of the IC4628 nebula is actually shown by Reipurth (2008; their Fig.8): the ionization pattern indicates clearly that its ionizing source lies South (or southwest) of the nebula, in agreement with Crampton & Thackeray (1971). Ionization in turn causes increased gas compression according to the Stromgren theory. On the other hand, the WISE image of Fig. 2 shows an arc-like region, suggestive of being pushed by a source in the North, close to IRAS 16562-3959. Since the two images, according to our unified view, show just two components of the same physical cloud, namely heated dust and ionized gas, the cloud medium is being compressed from both sides, which may be expected to lead to a rapid density increase, and enhanced star formation (see Gaczkowski et al. 2015) as indicated by our PMS candidates.

6. Conclusions

This study has revealed a large population of candidate PMS stellar members of the Sco OB1 association, on the basis of data from the wide-area VPHAS+ and VVV photometric surveys. In particular, the combination of a large studied region, deep and uniform multi-band photometry, and a carefully devised color selection has permitted to uncover about 4000 M-type candidate Sco OB1 members, spread over the entire association. Although not complete in mass (both towards solar-like masses, and towards the lowest stellar masses), this is the largest sample of candidate members of this star-formation region ever selected.

The individual clusters NGC 6231 and Tr 24, and the young H_{II} regions IC4628 and G345.45+1.50 have been shown to be subregions of the same star-forming Sco OB1 complex, falling along a likely ordered age sequence spanning almost 10 Myr, from the oldest NGC 6231 cluster to the youngest G345.45+1.50 cloud. The entire size of the complex is slightly over 50 pc. The distribution of member stars has an arc-like shape, which is consistently recovered using any of the available tracers (M stars, NIR-excess, UV-excess, Hα-emission stars, OB stars, X-ray sources). Five major stellar aggregates are found, coincident with the H_{II} regions G345.45+1.50 and IC4628, and clusters Tr 24, its southern extension, and NGC 6231, respectively, from North to South. The inferred total mass of ~8500 $M_{\odot}$ places the Sco OB1 complex among the most massive star-forming complexes in the Galaxy.

There is a remarkable difference between the compactness of the NGC 6231 cluster and the sparseness of its neighbor Tr 24. This latter was probably formed in a lower-density environment than NGC 6231, on the basis of the relative amount of residual dust and its dispersal timescales. Moreover, Tr 24 may be a good candidate as a cluster in the early dissolution phase, which our analysis method is particularly suitable to detect. The presence of the dense and massive cluster NGC 6231 nearby may

be accelerating the Tr 24 dissolution process via tidal effects, of which we also find traces. In the northern parts of the Sco OB1 complex, star formation occurs predominantly in smaller-scale groups, found from both optical and NIR PMS candidates and X-ray data.

The non-member contamination level derived for our M-type PMS candidates is found in the range 37–51%, averaged over wide regions. Locally, it depends on the richness and density of subclusters, and reddening. The average contamination is larger than that estimated from X-ray studies (5–10%), but the comparison is vitiated by the fact that these latter only refer to the denser cluster centers. X-ray studies with the sensitivity needed to detect M stars across the entire Sco OB1 complex would require an enormous observing time with current X-ray telescopes, and are therefore unfeasible in practice. Therefore, our technique is a valid substitute for the study of PMS populations covering wide sky regions, and is sensitive enough to be applied to star-forming regions as distant as the Sagittarius arm, like Sco OB1. It is thus also a promising tool for PMS cluster studies using next-generation photometric surveys (e.g., LSST).

We also suggest that the curved shape of the Sco OB1 complex may be related to its global rotation, inherited from the parent cloud. The upcoming data from the *Gaia* satellite will allow for this hypothesis to be tested.

Acknowledgements. We wish to thank an anonymous referee for his/her helpful suggestions, and Giusi Micela and Salvatore Sciortino for useful discussions. Based on data products from observations made with ESO Telescopes at the La Silla Paranal Observatory under programme ID 177.D-3023, as part of the VST Photometric Hα Survey of the Southern Galactic Plane and Bulge (VPHAS+, www.vphas.eu). Also based on data products from VVV Survey observations made with the VISTA telescope at the ESO Paranal Observatory under programme ID 179.B-2002. This publication makes use of data products from the Wide-field Infrared Survey Explorer, which is a joint project of the University of California, Los Angeles, and the Jet Propulsion Laboratory/California Institute of Technology, funded by the National Aeronautics and Space Administration. The scientific results reported in this article are also based on observations made by the *Chandra* and XMM-Newton X-ray Observatories. This research makes use of the SIMBAD database and the Vizier catalog service, operated at CDS, Strasbourg, France. We also make heavy use of R: a language and environment for statistical computing. R Foundation for Statistical Computing, Vienna, Austria (http://www.R-project.org/).

References

Albacete Colombo, J. F., Flaccomio, E., Micela, G., Sciortino, S., & Damiani, F. 2007, A&A, 464, 211
Albacete-Colombo, J. F., Damiani, F., Micela, G., Sciortino, S., & Harnden, F. R., Jr. 2008, A&A, 490, 1055
Avison, A., Quinn, L. J., Fuller, G. A., et al. 2016, MNRAS, 461, 136
Baraffe, I., Homeier, D., Allard, F., & Chabrier, G. 2015, A&A, 577, A42
Broos, P. S., Feigelson, E. D., Townsley, L. K., et al. 2007, ApJS, 169, 353
Caramazza, M., Micela, G., Prisinzano, L., et al. 2008, A&A, 488, 211
Caswell, J. L., & Haynes, R. F. 1987, A&A, 171, 261
Crampton, D., & Thackeray, A. D. 1971, The Observatory, 91, 109
Crawford, D. L., Barnes, J. V., Hill, G., & Perry, C. L. 1971, AJ, 76, 1048
Cutri, R. M., Skrutskie, M. F., van Dyk, S., et al. 2003, VizieR Online Data Catalog: II/246
Damiani, F. 2010, Star Clusters: Basic Galactic Building Blocks Throughout Time and Space, 266, 190
Damiani, F., Maggio, A., Micela, G., & Sciortino, S. 1997a, ApJ, 483, 350
Damiani, F., Maggio, A., Micela, G., & Sciortino, S. 1997b, ApJ, 483, 370
Damiani, F., Flaccomio, E., Micela, G., et al. 2003, ApJ, 588, 1009
Damiani, F., Flaccomio, E., Micela, G., et al. 2004, ApJ, 608, 781
Damiani, F., Micela, G., Sciortino, S., et al. 2006a, A&A, 460, 133
Damiani, F., Prisinzano, L., Micela, G., & Sciortino, S. 2006b, A&A, 459, 477
Damiani, F., Micela, G., & Sciortino, S. 2016, A&A, 596, A82
Damiani, F., Pillitteri, I., & Prisinzano, L. 2017, A&A, 602, A115
Drew, J. E., Greimel, R., Irwin, M. J., et al. 2005, MNRAS, 362, 753
Drew, J. E., Gonzalez-Solares, E., Greimel, R., et al. 2014, MNRAS, 440, 2036
Dutra, C. M., Bica, E., Soares, J., & Barbuy, B. 2003, A&A, 400, 533
Eiroa, C., & Casali, M. M. 1995, A&A, 303, 87
Feigelson, E. D. 1996, ApJ, 468, 306
Feigelson, E. D., Townsley, L. K., Broos, P. S., et al. 2013, ApJS, 209, 26
Flaccomio, E., Damiani, F., Micela, G., et al. 2003a, ApJ, 582, 382
Flaccomio, E., Damiani, F., Micela, G., et al. 2003b, ApJ, 582, 398
Flaccomio, E., Micela, G., & Sciortino, S. 2006, A&A, 455, 903
Fu, J. N., Sterken, C., Duerbeck, H. W., & Mennickent, R. E. 2003, A&A, 412, 97
Fu, J. N., Bouzid, M. Y., & Sterken, C. 2005, Astron. Nachr., 326, 349
Gaczkowski, B., Preibisch, T., Stanke, T., et al. 2015, A&A, 584, A36
Getman, K. V., Flaccomio, E., Broos, P. S., et al. 2005, ApJS, 160, 319
Getman, K. V., Feigelson, E. D., Townsley, L., et al. 2006, ApJS, 163, 306
Getman, K. V., Feigelson, E. D., Garmire, G., Broos, P., & Wang, J. 2007, ApJ, 654, 316
Getman, K. V., Broos, P. S., Kuhn, M. A., et al. 2017, ApJS, 229, 28
Guarcello, M. G., Prisinzano, L., Micela, G., et al. 2007, A&A, 462, 245
Guarcello, M. G., Micela, G., Damiani, F., et al. 2009, A&A, 496, 453
Gutermuth, R. A., Megeath, S. T., Myers, P. C., et al. 2009, ApJS, 184, 18
Guzmán, A. E., Garay, G., & Brooks, K. J. 2010, ApJ, 725, 734
Guzmán, A. E., Garay, G., Brooks, K. J., Rathborne, J., & Güsten, R. 2011, ApJ, 736, 150
Guzmán, A. E., Garay, G., Rodríguez, L. F., et al. 2014, ApJ, 796, 117
Haisch, K. E., Jr. Lada, E. A., & Lada, C. J. 2001, ApJ, 553, L153
Heske, A., & Wendker, H. J. 1984, A&AS, 57, 205
Heske, A., & Wendker, H. J. 1985, A&A, 151, 309
Lawrence, A., Warren, S. J., Almaini, O., et al. 2007, MNRAS, 379, 1599
Linsky, J. L., Gagné, M., Mytyk, A., McCaughrean, M., & Andersen, M. 2007, ApJ, 654, 347
Kalari, V. M., Vink, J. S., Drew, J. E., et al. 2015, MNRAS, 453, 1026
Korkov, A. V., & Orlov, V. V. 2011, Astron. Lett., 37, 248
Kuhn, M. A., Medina, N., Getman, K. V., et al. 2017a, AJ, 154, 87
Kuhn, M. A., Getman, K. V., Feigelson, E. D., et al. 2017b, AJ, 154, 214
Lada, C. J., & Lada, E. A. 2003, ARA&A, 41, 57
Laval, A. 1972a, A&A, 19, 82
Laval, A. 1972b, A&A, 21, 271
López, C., Bronfman, L., Nyman, L.-Å., May, J., & Garay, G. 2011, A&A, 534, A131
López-Calderón, C., Bronfman, L., Nyman, L.-Å., et al. 2016, A&A, 595, A88
MacConnell, D. J., & Perry, C. L. 1969, PASP, 81, 259
Meyer, M. R., Calvet, N., & Hillenbrand, L. A. 1997, AJ, 114, 288
Minniti, D., Clariá, J. J., Saito, R. K., et al. 2011, Boletín de la Asociación Argentina de Astronomía La Plata Argentina, 54, 265
Mottram, J. C., Hoare, M. G., Lumsden, S. L., et al. 2007, A&A, 476, 1019
Neckel, T., & Klare, G. 1980, A&AS, 42, 251
Perry, C. L., Hill, G., & Christodoulou, D. M. 1991, A&AS, 90, 195
Ramírez, S. V., Rebull, L., Stauffer, J., et al. 2004, AJ, 128, 787
Reipurth, B. 2008, Handbook of Star Forming Regions, Vol. II, 5, 401
Sana, H., Gosset, E., Rauw, G., Sung, H., & Vreux, J.-M. 2006, A&A, 454, 1047
Sana, H., Rauw, G., Sung, H., Gosset, E., & Vreux, J.-M. 2007, MNRAS, 377, 945
Schild, R. E., Hiltner, W. A., & Sanduleak, N. 1969, ApJ, 156, 609
Schild, R. E., Neugebauer, G., & Westphal, J. A. 1971, AJ, 76, 237
Sciortino, S., Micela, G., Damiani, F., et al. 2001, A&A, 365, L259
Seggewiss, W. 1968, Z. Astrophys., 68, 142
Siess, L., Dufour, E., & Forestini, M. 2000, A&A, 358, 593
Simon, T., & Dahm, S. E. 2005, ApJ, 618, 795
Skinner, S. L., Zhekov, S. A., Palla, F., & Barbosa, C. L. D. R. 2005, MNRAS, 361, 191
Spitzer Science Center 2009, VizieR Online Data Catalog: II/293
Sterzik, M. F., & Durisen, R. H. 1995, A&A, 304, L9
Strom, K. M., Strom, S. E., & Merrill, K. M. 1993, ApJ, 412, 233
Sung, H., Bessell, M. S., & Lee, S.-W. 1998, AJ, 115, 734
Sung, H., Sana, H., & Bessell, M. S. 2013, AJ, 145, 37
Townsley, L. K., Broos, P. S., Corcoran, M. F., et al. 2011, ApJS, 194, 1
Townsley, L. K., Broos, P. S., Garmire, G. P., et al. 2014, ApJS, 213, 1
Townsley, L. K., Broos, P. S., Garmire, G. P., et al. 2018, ApJS, 235, 43
van Genderen, A. M., Bijleveld, W., & van Groningen, E. 1984, A&AS, 58, 537
Wang, J., Townsley, L. K., Feigelson, E. D., et al. 2008, ApJ, 675, 464
Weidner, C., Kroupa, P., & Bonnell, I. A. D. 2010, MNRAS, 401, 275
Wright, E. L., Eisenhardt, P. R. M., Mainzer, A. K., et al. 2010, AJ, 140, 1868
Wright, N. J., Drake, J. J., Guarcello, M. G., et al. 2014, ArXiv e-prints [arXiv:1408.6579]

Appendix A: VVV-2MASS photometric calibration

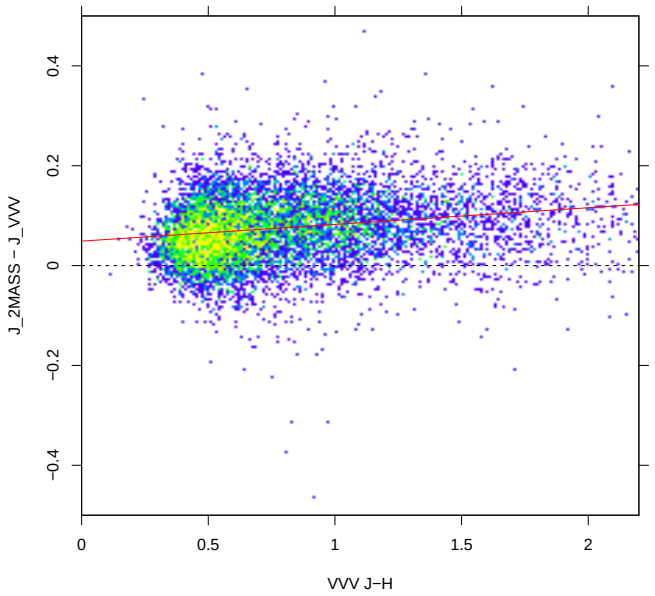

Fig. A.1. 2MASS-VVV comparison: difference $J_{2MASS} - J_{VVV}$ vs. VVV $J - H$ color (2-d histogram). The black dashed line represents $J_{2MASS} - J_{VVV} = 0$, while the red solid line is a best-fit to the data.

Using the set of sources common to both 2MASS and VVV catalogs, we compared their respective magnitudes and colors, to put all sources from our final combined catalog in the same system. There are slight but non-negligible differences in the photometry from 2MASS and VVV, which can be approximated satisfactorily using linear models. We consider only magnitudes with errors less than 0.07 mag, and colors with errors less than 0.1 mag.

The comparison between 2MASS and VVV J magnitudes, as a function of VVV $J - H$ color, is shown in Fig. A.1. A least-squares fit to the data has the form:

$$J_{2MASS} - J_{VVV} = 0.04902 + 0.03344\ (J - H)_{VVV}. \quad (A.1)$$

The 2MASS and VVV $J - H$ colors are directly compared in Fig. A.2. The linear best fit to the data has the form:

$$(J - H)_{2MASS} = 0.07523 + 1.06333\ (J - H)_{VVV}. \quad (A.2)$$

Similarly, Fig. A.3 shows the comparison between the respective $H - K$ colors, with the best fit here given by

$$(H - K)_{2MASS} = -0.06954 + 1.01811\ (H - K)_{VVV}. \quad (A.3)$$

Using these formulae, JHK magnitudes from the VVV catalog were converted to the 2MASS photometric system.

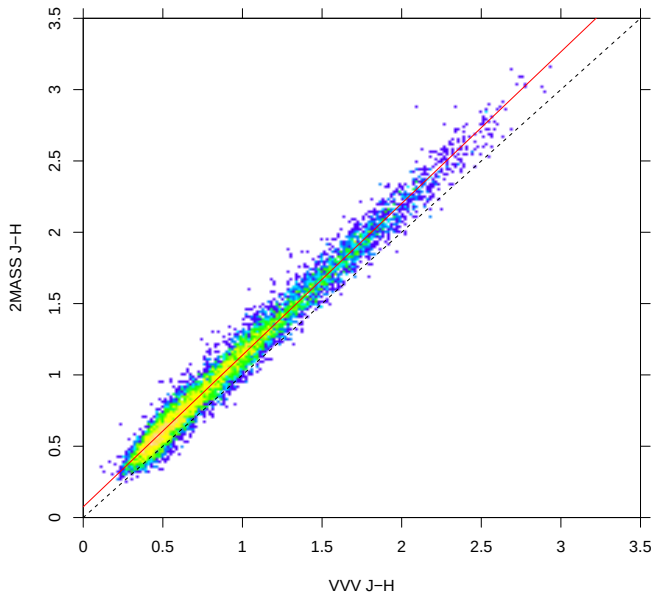

Fig. A.2. Comparison between $J - H$ colors from 2MASS and VVV. The black dashed line represents $(J - H)_{2MASS} = (J - H)_{VVV}$, while the red solid line is a best-fit to the data.

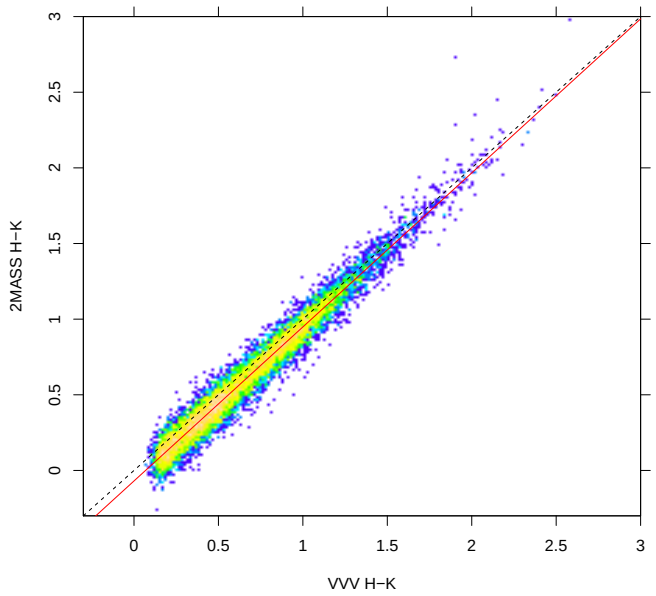

Fig. A.3. As in Fig. A.2, but for $H - K$.

Appendix B: Supplementary tables

Table B.1. *Chandra* ACIS-I X-ray sources in G345.45+1.50. Full table available at the CDS.

X-ray no.	CXO Id (CXOU)	RA (J2000)	Dec (J2000)	Pos. err. (arcsec)	Count rate (cts/ksec)	Rate error (cts/ksec)	VPHAS Id	r	$g-r$	$r-i$	J	$J-H$	$H-K$
1	J165852.8-400220	254.72007	-40.03892	2.66	0.724	0.143							
2	J165852.8-400135	254.72033	-40.02660	4.46	0.512	0.172					15.74	1.49	0.65
3	J165855.1-400224	254.72991	-40.04025	1.58	0.395	0.147	J165855.1-400224.2						
4	J165856.4-400530	254.73521	-40.09175	1.87	1.869	0.195	J165856.4-400530.4	15.40	1.59	0.90	12.95	0.76	0.22
5	J165857.5-400507	254.73975	-40.08551	1.33	0.685	0.121							
6	J165858.8-400150	254.74519	-40.03072	1.91	0.229	0.101	J165858.7-400150.2				10.08	0.62	0.22
7	J165900.9-400149	254.75401	-40.03036	1.98	0.544	0.159	J165901.0-400149.0	16.82		0.99			
8	J165901.9-400219	254.75827	-40.03868	1.51	0.376	0.122	J165901.9-400219.4	20.04		1.66			
9	J165903.3-400535	254.76408	-40.09307	3.10	0.344	0.116	J165903.1-400529.6	20.03		1.21	17.05	0.86	0.29
10	J165903.7-400635	254.76555	-40.10978	1.80	0.189	0.075							
11	J165904.5-400617	254.76886	-40.10489	1.40	0.505	0.146	J165904.4-400618.1	18.53	2.27	1.19	15.06	0.95	
12	J165905.2-400614	254.77194	-40.10389	1.33	0.150	0.074							
13	J165905.6-400623	254.77345	-40.10654	1.01	1.252	0.151	J165905.6-400623.6		0.68		11.78	0.28	0.31
14	J165905.8-395927	254.77433	-39.99090	1.94	0.179	0.083	J165905.9-395924.9						
15	J165906.0-400708	254.77540	-40.11916	1.58	0.324	0.107					14.96	1.00	0.48
16	J165906.2-400600	254.77625	-40.10003	1.30	0.533	0.106							
17	J165906.8-395903	254.77836	-39.98424	1.94	0.583	0.166							0.23
18	J165907.4-400912	254.78116	-40.15356	1.84	0.271	0.134	J165907.4-400913.3	18.88		1.41			0.30
19	J165908.0-400537	254.78334	-40.09385	1.01	0.511	0.151					16.75	2.78	1.62
20	J165908.6-401037	254.78591	-40.17699	1.98	0.311	0.170	J165908.5-401038.3	20.15		1.87	15.07	1.30	0.51

Table B.2. XMM-Newton EPIC X-ray sources in Tr 24. Full table available at the CDS.

X-ray no.	XMM Id (XMMU)	RA (J2000)	Dec (J2000)	Pos. err. (arcsec)	Count rate (cts/ksec)	Rate error (cts/ksec)	VPHAS Id	r	$g-r$	$r-i$	J	$J-H$	$H-K$
385	J165422.2-412148	253.59279	-41.36351	3.89	15.777	3.439							
386	J165442.1-412056	253.67548	-41.34911	5.76	5.784	1.363					9.21	0.04	0.05
387	J165500.0-412041	253.75034	-41.34476	2.77	3.579	0.781	J165500.2-412039.6	17.23	2.14				
388	J165428.6-412040	253.61951	-41.34454	5.44	7.007	1.474	J165428.8-412040.4	13.54	1.07		11.82	0.59	0.55
389	J165502.8-412009	253.76187	-41.33610	5.36	5.795	1.192	J165502.9-412010.7				14.63	0.71	0.17
390	J165526.2-412002	253.85930	-41.33398	4.03	3.451	0.800	J165526.3-412001.0						
391	J165427.6-411941	253.61530	-41.32824	1.44	3.014	0.718							
392	J165419.6-411937	253.58170	-41.32699	4.28	9.853	1.326	J165419.7-411935.7						
393	J165453.7-411937	253.72409	-41.32698	5.94	3.721	0.925	J165453.6-411936.1	17.00	1.72	0.94	14.60	0.78	0.21
394	J165524.5-411830	253.85210	-41.30859	4.43	2.464	0.676	J165524.7-411835.2	19.03		1.58			
395	J165415.4-411754	253.56430	-41.29852	4.03	2.976	0.688	J165415.5-411755.2	20.46		1.82			
396	J165502.6-411754	253.76104	-41.29834	4.75	5.857	0.960							
397	J165420.7-411743	253.58646	-41.29539	2.88	8.424	1.023							
398	J165410.8-411724	253.54540	-41.29024	2.70	3.414	0.717	J165410.8-411726.3	19.50	1.96	1.03			
399	J165502.6-411714	253.76113	-41.28731	2.84	2.528	0.572	J165502.7-411714.1	17.30	1.97		14.42	0.76	0.28
400	J165440.0-411645	253.66679	-41.27940	4.72	5.322	0.866					18.73	1.24	0.38
401	J165443.0-411629	253.67922	-41.27477	2.95	7.478	0.954					18.09	0.93	0.48
402	J165354.9-411606	253.47888	-41.26858	3.38	85.949	7.321							
403	J165409.4-411546	253.53954	-41.26296	2.45	4.322	0.758	J165409.5-411545.0	13.04	0.91		11.76	0.32	0.12
404	J165533.4-411540	253.88923	-41.26133	2.27	1.454	0.420	J165533.5-411539.8	16.99	1.66	0.91			

Table B.3. Optical and NIR photometry for M stars, and stars with UV or IR excess, or Hα emission. Full table available at the CDS.

Seq no.	RA (J2000)	Dec (J2000)	VPHAS Id	i	$r-i$	$r-H\alpha$	$g-r$	$u-g$	J	$J-H$	$H-K$	IR excess	Hα emission	UV excess
1	253.10967	-42.49575	J165226.3-422944.6	19.61	1.37	0.74			16.55	0.75	0.16			
2	253.22413	-42.47575	J165253.8-422832.6	17.33	0.79	0.37			15.11	0.82	0.44	Y		
3	253.21472	-42.45311	J165251.5-422711.2	17.18	0.91	0.44			14.44	1.47	0.63	Y		
4	253.43352	-42.43837	J165344.0-422618.1	19.54	1.51	0.78			16.07	0.82				
5	253.74475	-42.46394	J165458.7-422750.3	19.00	1.11	0.35			14.86	1.49	0.66	Y		
6	253.99296	-42.46397	J165558.3-422750.3	18.17	1.00	0.38			15.34	1.02	0.63	Y		
7	254.03561	-42.45187	J165608.5-422706.7	19.09	1.34	0.64			16.13	0.78	0.15			
8	254.15191	-42.47327	J165636.5-422823.8	18.51	1.03	0.42			15.45	1.19	0.77	Y		
9	254.28706	-42.48321	J165708.9-422859.7	20.19	1.13				16.85	1.94	1.18	Y		
10	254.36392	-42.46472	J165727.4-422753.0	19.44	1.09	0.35			16.07	1.40	0.75	Y		
11	254.39702	-42.48811	J165735.3-422917.1	18.74	0.98	0.37			16.07	0.73	0.51	Y		
12	254.65041	-42.49495	J165836.1-422941.7	19.28	1.25	0.35			15.59	1.04	0.74	Y		
13	254.81260	-42.45834	J165915.0-422730.0	18.26	1.25	0.47					0.60	Y		
14	254.94841	-42.49392	J165947.6-422938.1	19.77	1.42	0.50			14.63	2.46	1.13	Y		
15	254.98341	-42.44989	J165956.0-422659.5	19.49	1.22	0.45			15.38	1.92	1.06	Y		
16	252.69726	-42.41120	J165047.3-422440.3	17.94	1.28				15.03	0.86	0.25			
17	253.18205	-42.39847	J165243.7-422354.5	20.27	1.75				16.57	0.63	0.20			
18	253.19191	-42.40229	J165246.1-422408.3	15.78	0.86	0.33			13.46	0.64	0.49	Y		
19	253.32115	-42.37896	J165317.1-422244.2	20.08	1.61				16.48	0.80	0.32			
20	253.40177	-42.38816	J165336.4-422317.4	19.82	1.19	0.33			16.30	1.03	0.69	Y		